14-Years of Burn Scar Data from MODIS and Connections to PyroCb Development

W. Burke Beckley

A scholarly paper in partial fulfillment of the requirements for the Degree of Master of Science

May 2017

Department of Atmospheric and Oceanic Sciences

University of Maryland

College Park, Maryland

Advisor: Dr. Zhanqing Li

Abstract

Biomass burning has significant impacts on Earth's climate through emissions of aerosols and carbon into the atmosphere. Using monthly MODIS burn scar and active fire data, a 14-year data set of burn scar area in North America was analyzed. It was determined that, on average, 6.3×10^4 km^2 of land is burned annually. Fires are also instrumental in the development of pyrocumulonimbus clouds, or PyroCbs. These enhanced deep convective clouds have enough energy to overshoot the tropopause and inject smoke and water vapor into the lower stratosphere, where the aerosol particles and water can exist for months. To date, our understanding of PyroCbs is limited and the parameters for formation of PyroCbs is unclear. This project investigates the potential for fire size and burn duration as a factor for PyroCb development using known PyroCbs from 2013-2015. Results from the brief period studied here show that PyroCbs typically develop early in the lifetime of a fire and generally do not depend on fire size to initiate. In addition, a case study is presented to look at the parameters surrounding the development of several PyroCbs on July 31st, 2014. The case study is consistent with current theories on PyroCb formation and with the additional results presented here.

Table of Content

List of Figures

List of Acronyms

AVHRR – Advanced Very High Resolution Radiometer

BT – Brightness Temperature

CCN – Cloud Condensation Nuclei

CFSR – Climate Forecast System Reanalysis

CONUS – Continental United States

GHG – Greenhouse Gas

GIS – Geographic Information Software

GOES – Geostationary Operational Environmental Satellite

hPa – Hectopascal

LCL – Liquid Condensation Level

MODIS – Moderate Resolution Imaging Spectroradiometer

NCEP – National Center for Environmental Prediction

PyroCb – Pyrocumulonimbus Cloud

Section 1: Introduction

1.1 Emissions from Biomass Burning

The large-scale burning of biomass has a direct impact not only on local environments through the destruction of plant life, but also on the atmosphere through transport of gases and aerosols [Kaufman et al., 1998]. Atmospheric aerosols have a direct effect on radiation, acting to scatter and absorb incoming and outgoing radiation, and indirect effects, in which the aerosols act as cloud condensation nuclei (CCN) and increases the overall cloud albedo [Twomey, 1974]. Depending on the injection height of the aerosols, emissions can persist in the atmosphere for months, allowing for fires to impact globally, not just locally [Fromm et al, 2008].

Clouds, aerosols, and their effect on the Earth's Radiation Budget account for the largest uncertainty in future climate modeling [Boucher et al., 2013]. Therefore, quantifying the amount of biomass burning that occurs annually is valuable to not only forest management services or agriculture studies, but also to climate modelers who are trying to predict future climate outcomes and uncertainties. By some estimates, total global burned area amounts could be as high as 3.72 million km^2/year [Giglio et al., 2006]. In addition, biomass burning releases organic compounds and fine particulates into the atmosphere. Recent measurements estimate that biomass burning alone adds 400 Tg per year of non-methane organic compounds into the atmosphere. These gases influence the production of ozone and organic aerosols, which have a strong impact on human health and the radiation budget [Akagi et al. 2011].

Biomass burning and climate have a complex relationship; when one changes or shifts, the other will as well. For instance, the potential for wildfire and burn size is directly

related to weather parameters like wind speed, rain amount, and lightning. It is predicted that increased aerosol loading will lead to the suppression of precipitation through the direct microphysical effect of increased CCN [Ramanathan, 2001]. If rain rates decrease, specifically over land, vegetated areas become more susceptible to wildfires. The fires themselves then have a direct influence on climate change as they emit greenhouse gases (GHGs) and aerosols. A positive feedback loop involving wildfires and climate change is then created; as the effects of climate change become more pronounced, the number of fires increases, which increases the amount of GHG emissions and aerosols, which amplifies the initial climate change perturbation.

Wildfires can occur in some of the most remote areas of the world, and burn time can vary from several hours to several months in the case of extreme fires. Retrieving accurate information on burn data was nearly impossible before the advent of the satellite era since accounting for fires in isolated areas of the world was difficult. With satellite remote sensing systems, researchers are now able to observe fires and burn scars on a global scale at high resolution. One of the satellites that is best fitted to do this type of fire monitoring is the MODerate resolution Imaging Spectroradiometer (MODIS), as it has high temporal, spatial, and spectral resolutions [Kaufman et al., 1998]. Since their launch in 2001 (Terra) and 2002 (Aqua), the MODIS satellites have been taking measurements of the entire Earth four times per day and are well suited for studying long-term trends in biomass burning.

For the reasons described above, accurate and long-term records of wildfires and wildfire variability must be obtained. Their impact on climate change, atmospheric composition, and spatial variation need to be understood in order for climate models to be realistic.

1.2 PyroCb Detection and Development

As discussed, wildfires are directly connected to the atmosphere through the emissions of aerosols. These aerosols provide a means for cloud development by acting as CCN. For the most part, the aerosols from most surface based emissions are restricted to the troposphere; the lower 10-12 km of the atmosphere. Typical deep convective storms usually do not possess enough energy to pass through the tropopause and enter into the stratosphere due to the temperature inversion. However, there are some instances where the additional heat from fires can enhance convective thunderstorm development and produce what is known as a Pyro-cumulonimbus (PyroCb, for short) cloud. These PyroCbs are able to transport aerosols, ice, and water vapor into the stratosphere, a process once thought to be exclusive to volcanoes and cross-tropopause ascent in the tropics [Fromm et al., 2005; Thomason and Peter, 2006]. The emissions that are injected into the stratosphere may have a significant impact on climate studies and stratospheric chemistry. Currently, the number and effect of PyroCbs is thought to be underestimated [Peterson et al., 2017]. A thorough understanding of these PyroCbs is necessary in order for researchers to model the Earth's climate moving forward.

Until recently, the detection of a PyroCb was a manual process. There are two primary means of detecting a PyroCb. One, by observing aerosols in the stratosphere with a satellite platform and using a back-trajectory model (like HYSPLIT) to determine the source of the aerosols, or two, by analyzing satellite imagery obtained at the time of an event [Fromm et al., 2010; Fromm et al., 2005].

PyroCbs are identified by their Brightness Temperature (BT) value in the 11 μm channel. The intense convection, aided by the heat from the fires, transports water vapor higher into the atmosphere. As a result, PyroCbs produce large anvil ice clouds, which will

be at or below the homogeneous freezing level of -38°C in the BT_{11} channel [Wallace and Hobbs, 2006; Rosenfeld et al., 2007]. Using the Advanced Very High Resolution Radiometer (AVHRR), Rosenfeld et al. detected a PyroCb associated with a fire in Chisholm, Canada in 2001. The observed PyroCb overshot the tropopause by 2.5-3km and injected smoke into the lower stratosphere. This case has been studied in detail because of the excellent coverage of satellite data that coincided with the invigoration of the PyroCb. Figure 1 shows the AVHRR imagery from the PyroCb event. In the BT_{11} brightness channel, temperatures were as low as -66°C; well below the homogeneous freezing level. More interestingly, the deep convective core (indicated by C and D on Figure 1) of the PyroCb was not the coldest portion of the cloud. As the cloud overshoots into the lower stratosphere, it quickly adjusts to the surrounding temperature. Because of the temperature inversion in the stratosphere, this deep core will be warmer than the lower anvil, which is still located in the upper troposphere [Rosenfeld et al., 2007]. This study was fortunate in that there was a coincidental overpass of a high resolution (both spatially and spectrally) sensor that imaged at the time of convection. For many PyroCbs, this is not the case and a more reliable method must be developed to detect and quantify PyroCb activity annually.

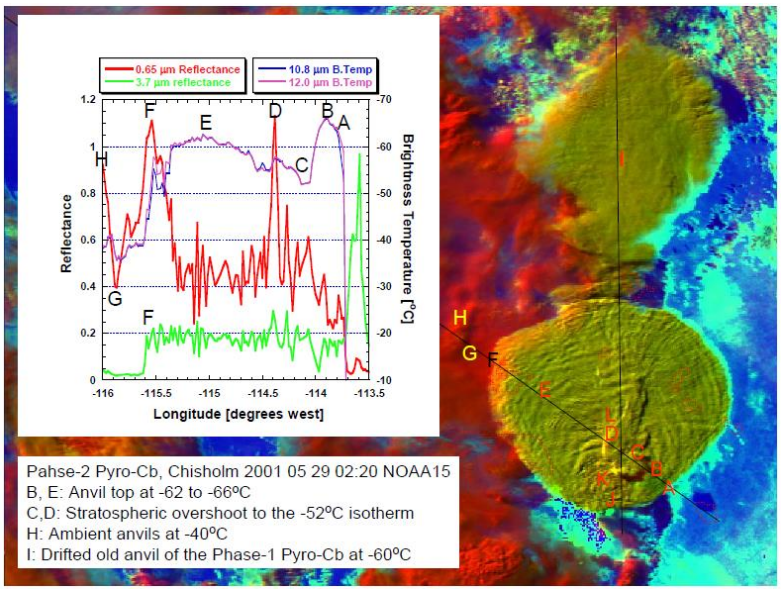

Figure 1: AVHRR imagery from a PyroCb in 2001. Image is an RGB composite, with visible in red, 3.7 µm in green, and 10.8 µm in blue. Cloud top temperatures are plotted on the left. The deepest part of the convection (C and D) do not correspond to the lowest temperature since they are likely in the lower stratosphere (Reference: Rosenfeld et al. 2007)

While satellites like MODIS and the AVHRR are useful for individual case studies of PyroCbs, satellites like the Geostationary Operational Environmental Satellite (GOES) system, may prove to be the platform necessary to determine how many PyroCbs occur annually. A 2017 study by Peterson et al. outlines a method that automatically detects PyroCbs with GEOS-W imagery. GOES-W is a geostationary satellite that images over the Western United States Canada and has a rapid revisit rate, making it the ideal sensor to monitor changes to clouds and cloud cover in short periods. The algorithm uses several channels from the GOES imager, notably the 4-μm, 11-μm, and 13-μm wavelength channels. The 11-μm channel is of particular importance because it identifies the cold clouds associated with deep convection. In their algorithm, they determine which clouds are associated with potentially intense convection by determining the value of the BT_{11} channel. For a potential PyroCb, BT_{11} must be less than -20°C. However, to be classified as intense convection that can inject into the lower stratosphere, these temperatures must be less than -35°C. Note that this is slightly warmer than the homogeneous freezing level of -38°C that was discussed earlier. The GOES BT_{11} are calculated over an area between 20 and 110 km^2 so a slightly warmer threshold is applied in order to account for subpixel convection [Peterson et al., 2017].

The algorithm developed by Peterson et al. was applied to data from 2013 to test the abilities and limitations. In particular, the algorithm is sensitive to small anvil size because the GOES pixels are large. Smaller PyroCb injections may go undetected. In addition, if there are extreme updraft velocities associated with the convection, smaller cloud particles are formed, which increases the difference between the 11- and 4-μm channels and results in a false positive for PyroCb detection. However, when applied to 88 intense wildfire cases in 2013, it was able to detect 31 individual pulses of PyroCbs; six of these PyroCbs

had previously gone undetected. The algorithm outlined in the Peterson et al. paper provides a means for more accurate quantification of PyroCb events, and defends the idea that PyroCbs are underestimated [Peterson et al. 2017].

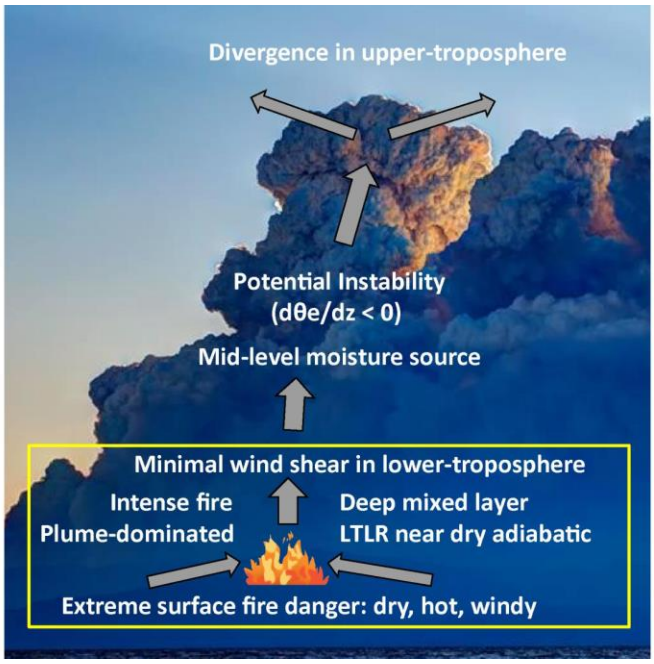

Figure 2: Conceptual model of PyroCb development as presented by Peterson et al. 2016. Hot, dry, windy conditions at the surface and a moist, unstable mid-level enhances convection to the UTLS. (Reference: Peterson et al. 2016)

Conditions for the formation of a PyroCb are still being constrained and is a field of active research. In 2016, Peterson et al. developed a conceptual model based on 26 PyroCbs that were observed in 2013; the same timeframe as the study for the detection algorithm. The researchers investigated the meteorological conditions associated with each of the PyroCbs to determine the similarities or necessary parameters that need to be met in order for one of these convective systems to develop. Figure 2 shows the conceptual model developed from that study. They found that PyroCbs develop in synoptic conditions that are already prone to the development of deep convection. At the surface level, hot, dry, and windy conditions drive the fire to become more intense. As the fire intensifies, additional heat and smoke are added into the atmosphere, providing the eventual trigger for PyroCb development. The lower tropospheric layer is typically dry and unstable, with low wind shear. The low wind shear and unstable conditions allow plumes to develop, which increases the probability that the plume will reach higher than the lifting condensation level (LCL) [Peterson et al. 2016].

Above the lower level, mid-atmospheric moisture is vital to the development of a PyroCb. While the low level must be dry and hot, the mid-troposphere must contain sufficient moisture in order for the PyroCb to continue lifting. Condensation occurs because of the additional moisture, which causes latent heat to be released. The latent heat drives the plume higher into the atmosphere and allows the PyroCb to develop. A connection to local terrain and elevation of the surface level also exists as low surface elevation fires require a large potential instability and moisture since the plume must travel a greater distance in order for a PyroCb to inject into the stratosphere. Higher elevation fires, therefore, have a greater chance to develop into a PyroCb. Finally, upper level dynamics may also play a part in the formation of PyroCbs. If a jet is located above an intense fire, the lower level convergence/upper level divergence associated with the right jet entrance region may aid PyroCb development for fires that are not situated on topography conducive to intense plume activity [Peterson et al. 2016; McRae et al. 2015].

1.3 Objectives of this Study

Quantifying the amount of biomass burned is vital to not only land management practices, but also to understanding the global carbon cycle, land use/land cover changes, and patterns within the biomass burning cycle. Previous studies have developed burned area datasets in order to estimate the total burned area globally or regionally [Giglio et al. 2006; Pu et al. 2006]. The Pu et al. study from 2006 produced a dataset for North American forest fires and burned area over a 12-year time span. While the study was over a significant period, it used the AVHRR sensor which is limited to a 1 km resolution pixel size. The Giglio et al. paper produced a dataset of global burned area using the more advanced MODIS platform, which has a resolution of 500 m. However, this study focused

on a few years of data only, spanning from 2000 to 2005. In the study conducted here, a dataset of North American burn scar area is presented which uses the MODIS platform and data from 14-years of collection; from 2002 to 2015.

While the necessary atmospheric dynamic requirements for PyroCb development are being constrained, the relationship between PyroCb invigoration and fire size and duration are not well understood [Peterson et al. 2016]. Using the burn scar area dataset from this study and the PyroCb library maintained by the PyroCb working group, connections between the total burn area of fires, length of a fire, and PyroCb development are presented. In addition, a case study of several PyroCb events on single day is examined. The focus of the case study is to understand the meteorological conditions that surrounded the creation of multiple PyroCbs within a small area and what conditions were observed during development. With the combined burned area dataset and PyroCb library, this study aims to constrain more unknowns surrounding PyroCb development, namely the size and intensity of a forest fire that can induce such intense convection.

Section 2: Study Area, Data, and Methodology

2.1 Area and Time Span of Study

Following the research of Pu et al., this study concentrates on forest fires in North America for the majority of the extent of MODIS collection. North America was the focus of this study for several reasons. For one, forests make up much of the land in North America. 45% of Canada and 32% of the United States are forest, covering 7.33 million km^2 of land. The large amount of forest cover makes North America particularly susceptible to biomass burning, especially during dry and hot seasons. In addition to forest

fires, North America experiences many PyroCbs annually due to favorable meteorological conditions (i.e. dry, hot, windy surfaces and moisture in the middle atmosphere) [Fromm et al. 2010; Peterson et al. 2016]. Therefore, when attempting to connect forest fire size and PyroCb development, North America is an ideal location as the land cover and synoptic conditions are favorable for both phenomenon. Specifically, this study focuses on the continental United States (CONUS) plus Alaska, and Canada up to 70°N.

As previously stated, this study examines forest fires and burn scars between the years of 2002 and 2015. Only the months of May 1 to October 31 were used in these years. These months are considered to be the burning season for North America and follows work from previous biomass burning studies [Pu et al. 2007].

2.2 Data Sets Used

Multiple data sets were utilized to estimate burn area, burn duration, land cover type, PyroCb development, and meteorological conditions. MODIS image products provided the data for the burn scar area and burn duration. There are currently two MODIS platforms in orbit, MODIS/Terra and MODIS/Aqua. Both satellites are in sun-synchronous orbits; Terra passes overhead at 10:30 AM local time, while Aqua passes at 1:30 PM. Terra was launched in 1999 and Aqua followed shortly after in 2002. For the sake of consistency, this study used only imagery from overlapping collection times (2002-2015).

One of the MODIS products used was the MCD14ML dataset, produced and maintained by the University of Maryland. The MCD14ML is 1km resolution monthly composite data, which provides geographic coordinates of fire pixels, the satellite that detected the fire, the date of the month the fire occurred, the brightness temperatures from

bands 21 and 31, fire radiative power, and confidence of detection. Because this was a monthly composite dataset, this data format was chosen over the other MODIS fire products such as the MOD14A1. The data is processed as a plain ASCII text file in a Geographic Information System (GIS) software to allow for easy data manipulation [Giglio, 2015]. To determine if a pixel contains a fire or not, the MODIS algorithm calculates the differences in brightness temperatures between channel 21 (the 4-μm band) and channel 31 (the 11-μm band). The infrared portion of the EM spectrum is useful for characterizing fires, as fires emit strongly in the infrared [Dozier, 1981; Matson and Dozier, 1981]. Each channel has a different response to fires, however, and the 4-μm band is more sensitive to fire emissions. Therefore, it is the magnitude of the increase in channel 21 (both absolute and relative to channel 31) that characterizes the fire detections for a scene [Giglio et al. 2003].

The second dataset derived from MODIS was the MCD45A1 burn scar area product. This level 3 monthly-tiled product provides pixel level burning information at a 500 m resolution and estimates the date that the burning occurred. Reflectance values from several MODIS bands are compared against past observations of daily reflectance values. The seven land surface reflectance bands (MODIS bands 1-7) are atmospherically corrected and any bad quality pixels (due to high aerosol, snow, cloud, or non-land) are rejected from the batch of comparison pixels. To discriminate between unburned and burned pixels, research determined that band 5 (1230 – 1250 nm) and band 2 (841 – 876 nm) were best suited for burn scar detection [Roy et al. 2002, 2005]. In order to account for variations in angle, a bidirectional reflectance distribution function (BRDF) is applied. Since a BRDF model accounts for changes to the viewing angle, burned/unburned areas can be determined off nadir [Justice et al., 2006].

A simplified land cover type was included in this study. An eco-region map based on the macroclimate was developed by Bailey and characterizes broad domains. Figure 3 is a visualization of the four eco-domains that span North America. The four regions are polar, humid temperate, dry, and humid tropical [Baily, 1998]. These domains have been used in the previous research to divide burn areas, as different domains may be susceptible to various rates of burning [Pu at al. 2007].

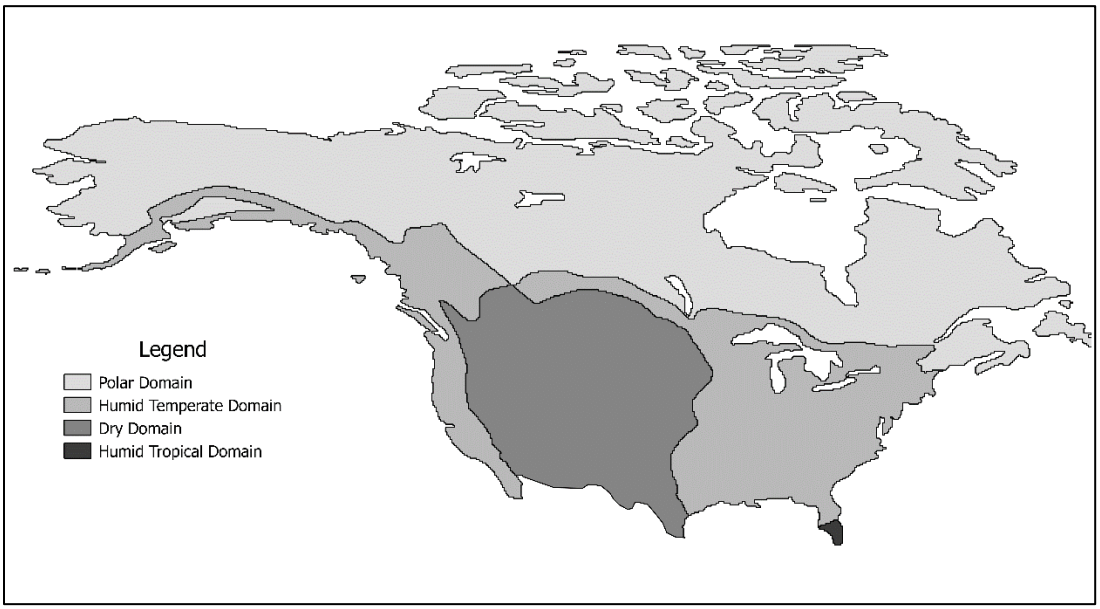

Figure 3: The four eco-domains of North America, as presented by Baily, 1998.

An inventory of detected PyroCbs has been maintained over the past few years by a PyroCb working group, which includes researchers from academia and government agencies. This working group aims to monitor and record PyroCb activity, including date of injection, BT of the plume, location the PyroCb originated from, and the height of the tropopause sounding data was available. However, these records have not been maintained for an extensive period. In this study, PyroCb data from 2013 to 2015 are utilized which was the extent of the records at the beginning of this research.

In the span of this study, there were roughly 130 PyroCb events in North America alone. Table 2 in the Appendix lists the events by date, includes the latitude/longitude, and name of the fire if available. All PyroCbs in the domain occurred between May 1 and October 31; the extent of the study and the peak burning season for North America. Efforts are currently underway to extend the timespan of the database.

For the PyroCb case study, GOES West imagery was obtained to monitor the development of the convection over the course of a day. The GOES W satellite is a geostationary sensor with a subsatellite point of 135°W allowing for collection over western CONUS and parts of western Canada. Based on Table 2, most PyroCbs in North America are located within this region, so this sensor is well suited for PyroCb detection in North America. Four of the GOES bands provided detailed information regarding the fire locations (shortwave band), atmospheric moisture (water vapor band), and cloud development (visible and infrared bands). Applications of the GOES sensor for PyroCb detection has been done on multiple occasions and it is one of the most useful satellites for monitoring and categorizing PyroCbs [Peterson et al. 2017; Fromm et al. 2010]

Meteorological parameters during the case study were also examined. Studying the synoptic conditions surrounding a PyroCb event allows for a deeper understanding of why the event took place. Atmospheric soundings determined from radiosondes launched around the time and location of the PyroCbs provide vertical dew point and actual temperature throughout the atmosphere. The measurements from the soundings allow for calculations of humidity, stability, and convection potential.

Radiosonde data is usually collected twice a day only in the United States; once at 12Z and once at 00Z. Therefore, if the PyroCb events occur between those collection times,

the necessary parameters required to understand the state of the atmosphere need to be obtained through data assimilation. The Climate Forecast System Reanalysis (CFSR) is an hourly, half-degree product that combines observations from in-situ and satellite data to create modeled states of the land-ocean-atmosphere interactions. The data was obtained from the National Center for Environmental Prediction (NCEP), a division within NOAA (https://www.ncdc.noaa.gov/data-access/model-data/model-datasets/climate-forecast-system-version2-cfsv2). Utilizing the 3-D pressure level data (PGB) allows for examination of thermodynamic variables in the vertical, including temperature, pressure, and humidity. CFSR was chosen over other reanalysis datasets because it is the most recent reanalysis from NOAA/NCEP.

Utilizing satellite observations, in-situ measurements, and modeled data allows for a thorough investigation into active fires and burn scars, PyroCb activity, and the meteorological conditions surrounding the development of those PyroCbs. It is the goal of this paper to connect the observations and understand if there is a relationship between fire size, fire duration, and PyroCb initiation.

2.3 Methodology

2.3.1 Burn Scar Area

The MODIS data, both the MCD45A1 and MCD14ML, were processed in a GIS software program called QGIS. This software provides many of the same features as the well-known ArcGIS, including displaying shapefiles, ingesting points with geographic coordinates, and working in various projections. The MCD45A1 products are produced in the Plate-Carrée equirectangular projection, which is widely used in NASA datasets because of the basic relationship between an image pixel and a corresponding geographic

position. The MCD45A1 monthly product is created and maintained at the University of Maryland. For ease of use, the monthly datasets are divided into subsets that cover different continental sections. Figure 4 shows the global coverage of the MCD45A1 monthly product [Boschetti et al., 2013]. Since North America is the focus of this study, only Boxes 1, 2, and 3 were used to generate the burned scar estimates. The latitude/longitude extent of the boxes are displayed in Table 1. Notice that there is significant overlap between boxes 2 and 3, and slight overlap between boxes 1 and 2. In order to ensure that burned areas were not counted twice due to overlap, box 2 was reduced to a minimum latitude of 50°N and a minimum longitude of -141°W. These reductions are noted in Table 1 in parentheses after the original value. Each of the bounding boxes also overlap into regions that are not part of this study (i.e. box 3 extends into Central America and box 2 extends into Greenland). The domains were reduced to the area extent of North America using a clipping tool within the GIS software that excluded any points outside of desired area of study.

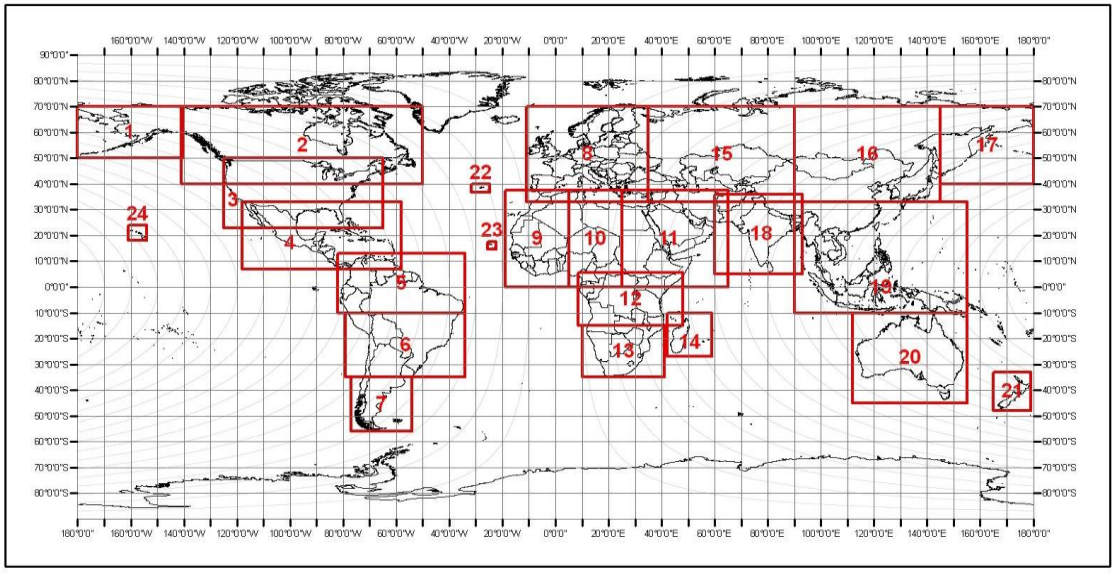

Figure 4: Coverage of the shapefile datasets produced by the University of Maryland. Boxes 1, 2, and 3 were used for this study (Reference: Boschetti et al, 2013).

Window #	Coverage	Min Long	Max Long	Min Lat	Max Lat
1	Alaska	-180	-140.5	50	70
2	Canada	-141.5 (-141)	-50	40	70 (50)
3	CONUS	-125	-65	23	50

Table 1: Bounding coordinates for the domains used in this study. Original extents are listed, and the reduced Canadian extents are noted in parentheses.

In order to calculate the area of burned land annually, monthly totals for May through October were estimated for each of the bounding box domains. The basis of this estimation relies on the fact that each of the pixels in the MCD45A1 are 500 meters in resolution, meaning that each pixel has an area of .25 km^2. For each bounding box, the number of burned scar pixels was calculated and then multiplied by .25 km^2 to retrieve the total burned area per bounding box per month. Since any overlap between the bounding boxes was eliminated by the first processing step, the sum from all three bounding boxes represents the total burned area in North America for that respective month. Burned area was also partitioned into the four eco-domains (Figure 3) that were previously described.

2.3.2 Calculating Burn Area for Fires Inducing PyroCbs

One of the primary goals of this research was to understand if a connection exists between a fire's start date, the burn duration of a fire, and PyroCb development as that is currently unknown [Peterson et al. 2016]. Since the dates of PyroCbs are known from the database spanning 2013 to 2015, the only step that needed to be performed was determining when the fires that initiated the deep convection began. Both of the MODIS datasets (MCD45A1 and MCD14ML) are monthly products. However, they contain daily information at the pixel level; each data point contains within it the date that the active fire or burn scar was detected. For each of the PyroCb cases, the fires and burn scars that were associated with the PyroCb were examined in detail. The start date of a particular fire associated with a PyroCb was determined by the earliest detection of a fire in the

surrounding region. Fire start date was taken from either the burn scar product or the active fire product; whichever detected the fire first.

Fire start dates calculated here are not exact, but estimates as both products have limitations. For example, if a fire is too small for detection at the beginning the burning lifetime, or if cloud cover prevented the satellite from observing an active fire or scar, then the date of initiation would be incorrect. Therefore, the fire start date described here is truly the date of first detection from a satellite. While the resolution of these products is between 500 and 1000 m, the sensitivity of the infrared bands allows for detection of fires even if they are sub-pixel. The 4-μm band, for example, is able to detect fires that are 2.5% of the pixel size if the fire is hot enough [Justice et al., 2006]. For the most part, this method is reliable as most of the PyroCbs had detectable fires or burn scars before the initiation of convection. However, several PyroCbs were not associated with a nearby fire. This could be explained by short-lived fires that were under cloud cover before and after the initiation of pyroconvection.

Determining the total burn duration of a PyroCb fire was more involved than determining the first detection date from satellite data. First, each PyroCb was mapped using the GIS software and plotted on top of the burn scar product. Then, the duration of the fire was found using the burn scar product. The last day of an observed burn scar was categorized as the "end date" of the fire, even if the active fire product had detections after the last burn scar. The main interest for the burn duration was how much area the fires had consumed during their lifetime, so it was deemed appropriate to only use the burn scar product as the end date. It may seem contradictory to use both the active fire product and the burn scar product for the start date, but only the burn scar data for the end date.

However, because PyroCbs would often occur near the start date of fires before any burn scaring had been detected, the active fires needed to be used to constrain the start date of PyroCb fires.

With a length of burning now established, burn scar area for each of the PyroCb fires was estimated. GIS software allowed for area calculation using the same technique used to calculate total area of burn scar, but only the burned pixels for the PyroCb fires were selected. The process to determine area was manually intensive because some of the fires were small and lasted a few days only, while some of the fires that produced PyroCbs engulfed hundreds of square kilometers and burned for months. In addition to estimating the total area of a PyroCb producing fire, for each PyroCb, the total area burned until the date of the PyroCb was also calculated. Constraining burn scars in this fashion allows for investigations into burn size or fire intensity before a formation of a PyroCb.

Section 3: Results and Discussion

3.1 Burn Scars in North America: 2002 – 2015

The data and method described above allowed for calculations of the total burn scar area between 2002 and 2015. The burn scars observed in MODIS monthly data are presented and reviewed in terms of their annual variation within the fire season (May through October) and also within their respective eco-domains. The analysis performed here is in line with previous work that reviewed a long-term dataset of burn scar area [Pu et al. 2007].

The spatial distribution of burn scars is vast over North America (Figure 5). To allow for visibility, the burn scars on the map are shown larger than their actual size. Previous research concluded that burning amount rises through the summer until peaking in July and then decreasing through October [Pu et al. 2007]. The work here shows a general agreement in terms of trends with the previous work. Figure 6 is a representation of the average, maximum, and minimum burn scar area per month for the 14 year timespan of the

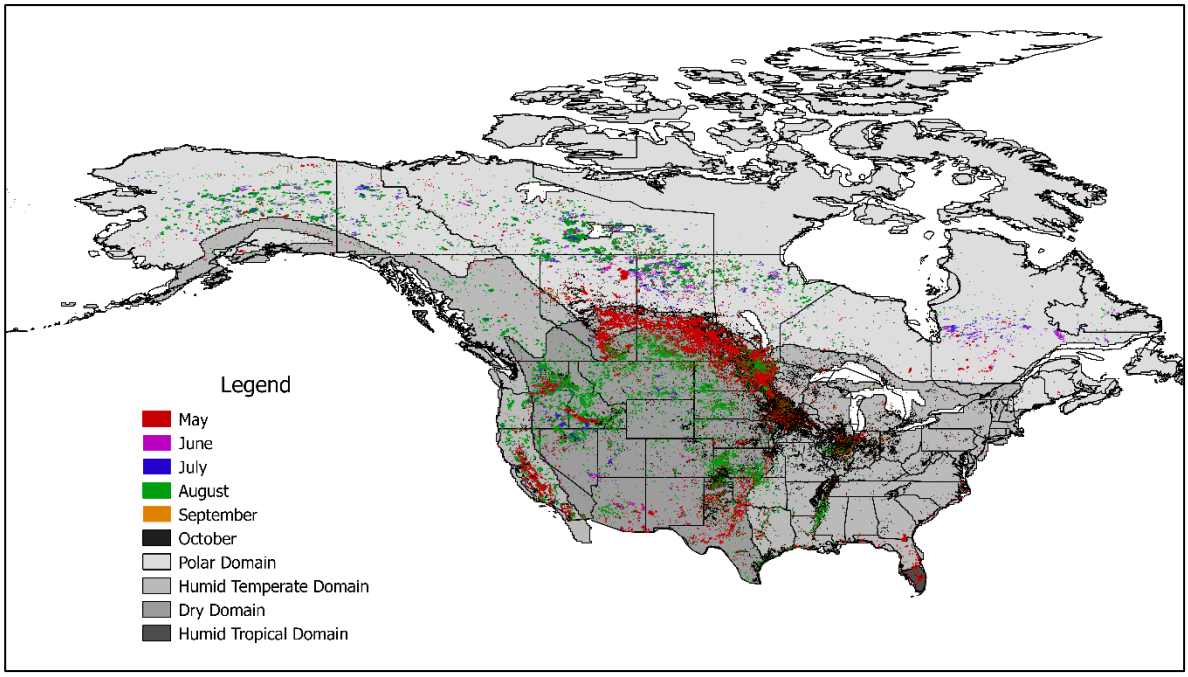

Figure 5: Burn scars by month for 2002 to 2015 over the eco-domains. Burned area pixels are shown larger than actual size in order to visualize on the map.

study.

July is typically the month with the most burned scar area, averaging 1.9 x 10^4 km^2 per year. May experienced the lowest amount of burning on average with 3.8 x 10^3 km^2 per year. The temporal variations of the burn scarring described in Figure 5 can be observed primarily in Northern Canada and Alaska. These regions (the polar eco-domain) experience the highest amount of burning in June, July, and August.

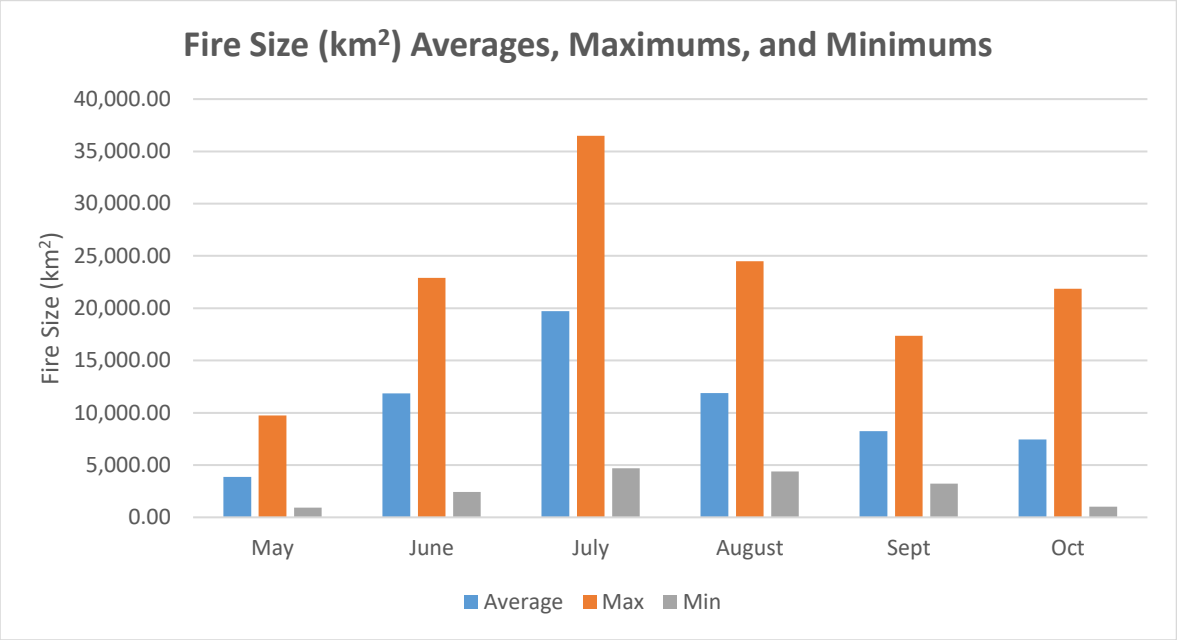

Figure 6: Fire sizes (average, maximums, and minimums) between 2002 and 2015. July experienced the most burning on average (1.9 x 10^4 km^2) and May experienced the least amount (3.8 x 10^3 km^2)

Climatological effects can explain much of the variation in burning. After winter, as the sunlight returns to the Northern Hemisphere, the snow and ice melts, exposing the vegetation underneath. The now exposed vegetation is then susceptible to catching fire, through either natural means (such as lighting) or anthropogenic (human-induced) causes.

Research has shown that there is a positive correlation between lightning occurrence and forest fires in Canada and Alaska [Flannigan and Wotton, 1991]. During the summer months of June, July, and August, lightning occurs more frequently than other seasons and can account for a large percentage of the burned area [Wierzchowski et al., 2002; Kasischke et al., 2002]. Aside from lightning, relative humidity can affect fire initiation. In Canada, Alaska, and the southwestern United States, relative humidity is the lowest in July [Pu et al., 2007]. In Figure 5, the effects from a lower relative humidity can be seen across those three areas as burning increases during the summer months.

Figure 7a is similar to Figure 5, but displays burned scar pixels by year in North America rather than by month. Through analysis of the MODIS burn scar product, yearly totals of burning were estimated. From these results, burning from 2002 – 2015 averaged

6.3 x 10^4 km^2 per year. A maximum occurred in 2014 as an estimated 9.0 x 10^4 km^2 of area was detected as burned by the MODIS product. A minimum detected burn scar area occurred in 2009, with 2.8 x 10^4 km^2 of land burned. Figure 7b displays the temporal variation of the burning by year between 2002 and 2015. Since the minimum in 2009, burn scar area have generally increased, as every year except 2011 experienced more burn scar detections than the average for the 14-year timespan.

Compared to previous similar research, the results from this study were high, though within the same order of magnitude. In the work by Pu et al., which estimated burn area over a 12-year timescale on a 1 km resolution from AVHRR measurements, the

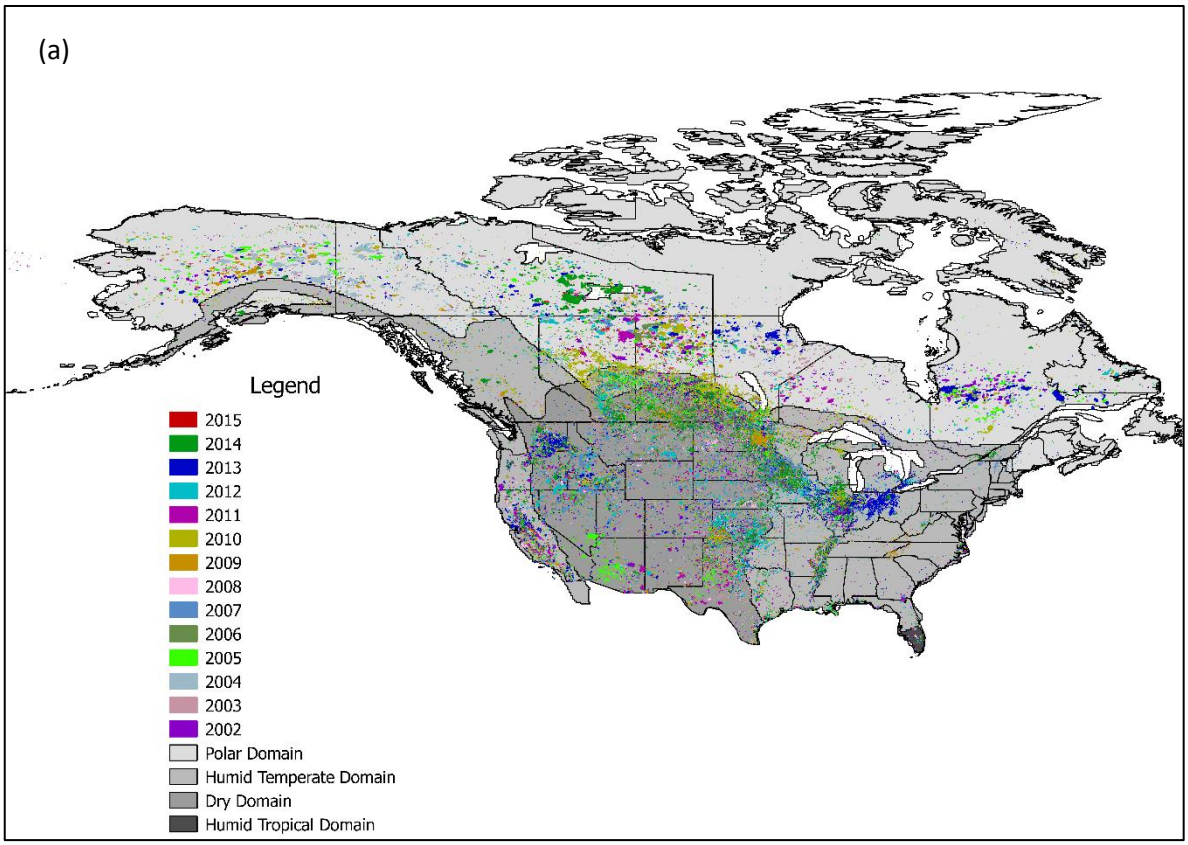

Figure 7a: Burn scars by year from 2002 to 2015. Burned area pixels are shown larger than actual size in order to visualize on the map.

Figure 7b: Total burn scar area in km^2.

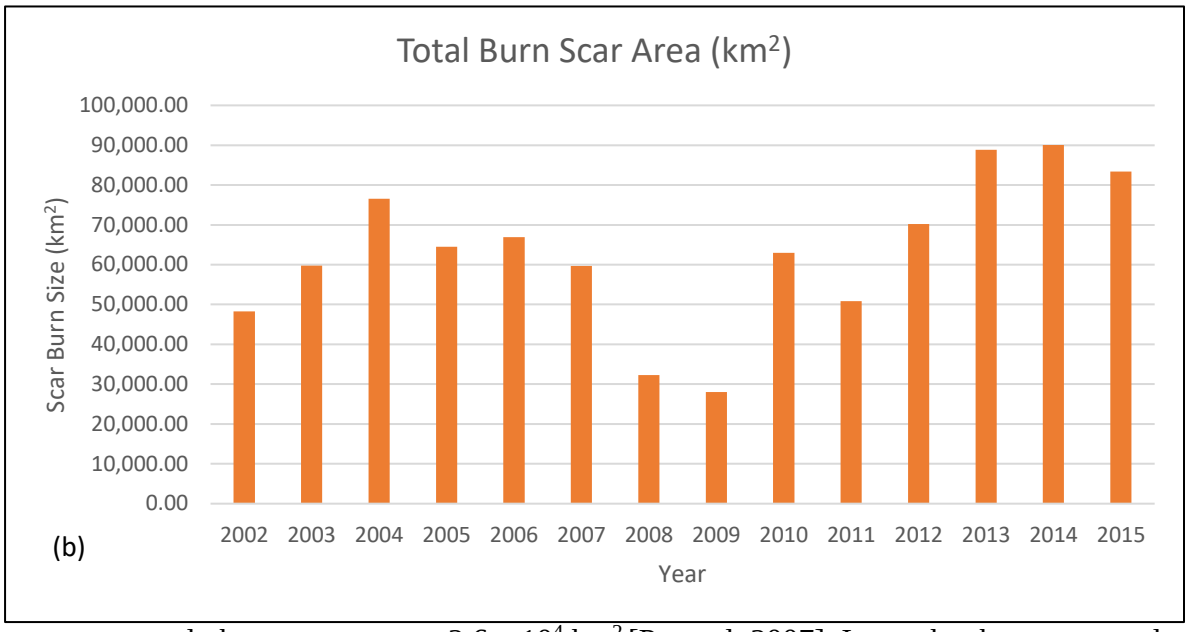

average yearly burn amount was 2.6 x 10^4 km^2 [Pu et al. 2007]. In another burn area study from Giglio et al. conducted in 2006, it is estimated that burn area in North America was 4.3 x 10^4 km^2 in 2002, 3.8 x 10^4 km^2 in 2003, and 5.2 x 10^4 km^2 in 2004 [Giglio et al., 2006]. Compared to the estimates from figure 7b, those results have a difference of 11%, 43%, and 37%, respectively. The 2006 study used an early MODIS burn scar detection algorithm; though at that time they only used data from MODIS/Terra. Both of the earlier studies relied on one satellite only to monitor burn scar area. The method used in the research for this paper relied on two satellites, or four observations per day. It is possible that the additional coverage of satellites resulted in more burn area being detected, as a single sensor would be limited more by cloud cover or poor visibility. In addition, burn area may be underestimated in the earlier studies for certain regions. For example, Figure 8 shows the annual variation in burn scar area by eco-domain from the 2007 Pu et al. study. The dry eco-domain results are considerable less than the estimations from this research, which is shown in Figure 9. The

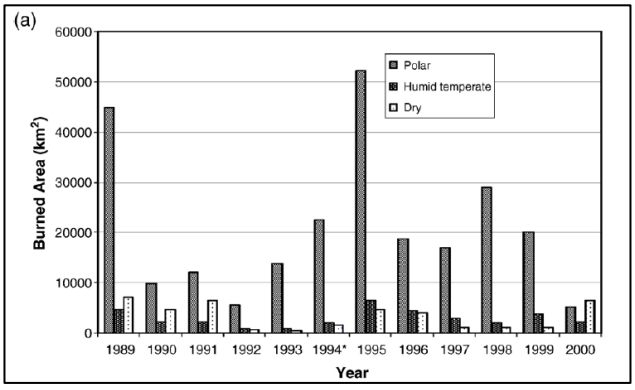

Figure 8: Total burned areas in various years by eco-domain.

current MODIS product may detect burn area over these domains more effectively than the algorithm for the AVHRR. Underestimation from the dry eco-domain may also be accounting for differences from the 2006 Giglio et al. study. In their research, they prescribed all of CONUS as a temperate forest. The year with the largest difference between the Giglio et al. study and this research was in 2003 where a 43% was seen. The

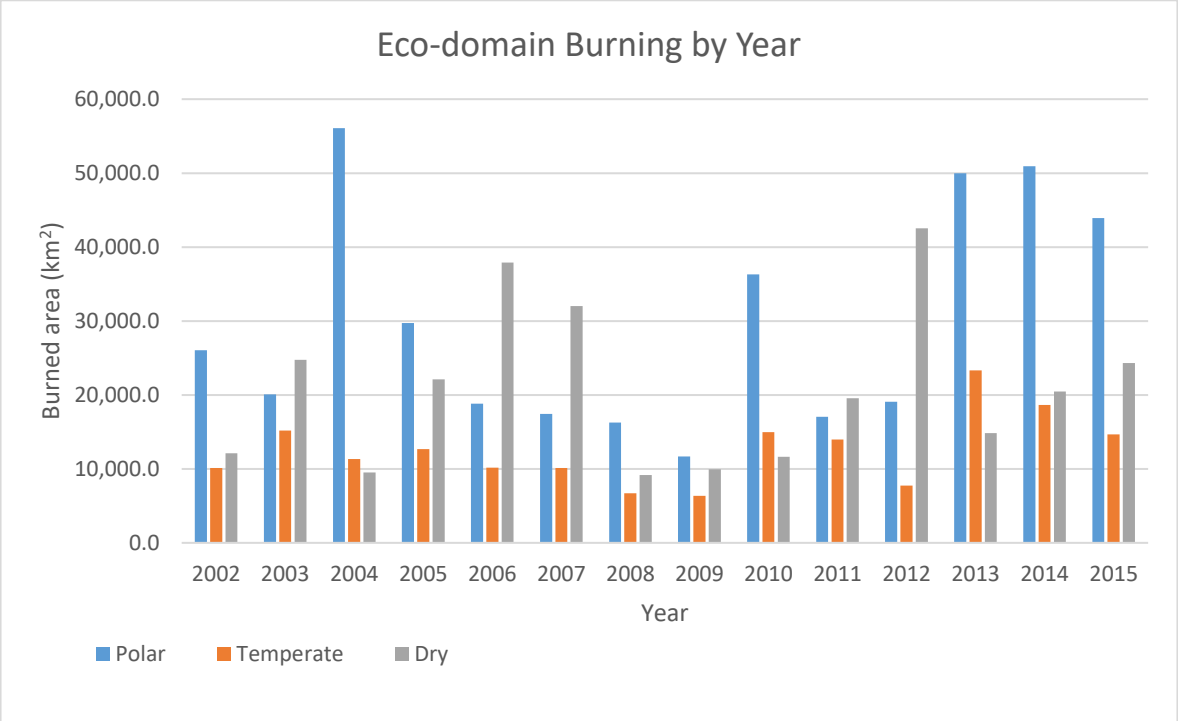

Figure 9: Total burned area by year between 2002 and 2015 by Eco-Domain.

large difference coincides with a year where a smaller amount of polar burning occurred (in both the Giglio et al. work and in this work) and a larger amount of burning in the dry eco-domain. By including more types of domains, the accuracy of burn scar estimates may increase.

Large fires tend to dominate burning in certain years, especially in Canada. In fact, the polar eco-domain experienced the most burning in every year except 2003, 2006, 2007, 2011, and 2012 when the dry eco-domain was dominant. Figure 9 is the amount of burn scar in each of the respective eco-domains. The humid tropical region is not displayed as

burning was minimal there; in only two years did burning in that region surpass 100 km^2 (2006 and 2011). The trend in the results agreed with previous research by Pu et al. in 2007, which determined that the polar eco-domain had the most burned area between 1989 and 2000 [Pu et al., 2007]. However, as was discussed earlier, the burn area estimates from the dry eco-domain region was considerably less in the 1989 – 2000 timespan than in the 2002 – 2015 timespan.

3.2 Connections between fire size, duration, and PyroCb development

PyroCbs have been observed and studied at length from large fires that engulf hundreds to thousands of hectares of vegetation [Peterson et al. 2015; Fromm et al, 2006; Rosenfeld et al. 2007]. Despite the number and depth of these studies, the minimum fire intensity, minimum burn duration, or minimum burn area that is required is still unknown [Peterson et al. 2016]. The next results will examine the relationship between PyroCbs in North America from 2013 – 2015, with a focus on the age of the fire and total area burn up until the formation of the PyroCb.

Figure 10a shows the spatial distribution of the ~130 detected PyroCbs between 2013 and 2015 overlaying the four eco-domains. Many of the fires resulted in multiple injections, causing overlap on the map shown on Figure 10a. As a reminder, the list of PyroCbs was provided in Table 2. Figure 10b represents the locations of PyroCb convection by eco-domain from 2013 to 2015. The polar region in Northern Canada and Alaska experienced the most PyroCb events with 58 over the course of the three-year timeframe. Fires in the humid temperate region initiated 41 PyroCbs, while the dry eco-domain produced 34. The humid tropical region of Florida produced no PyroCbs over the

course of the study. Spatially, most PyroCbs were observed in the Western United States and Canada, though a few Canadian PyroCbs were detected as far east as the Manitoba and Quebec provinces.

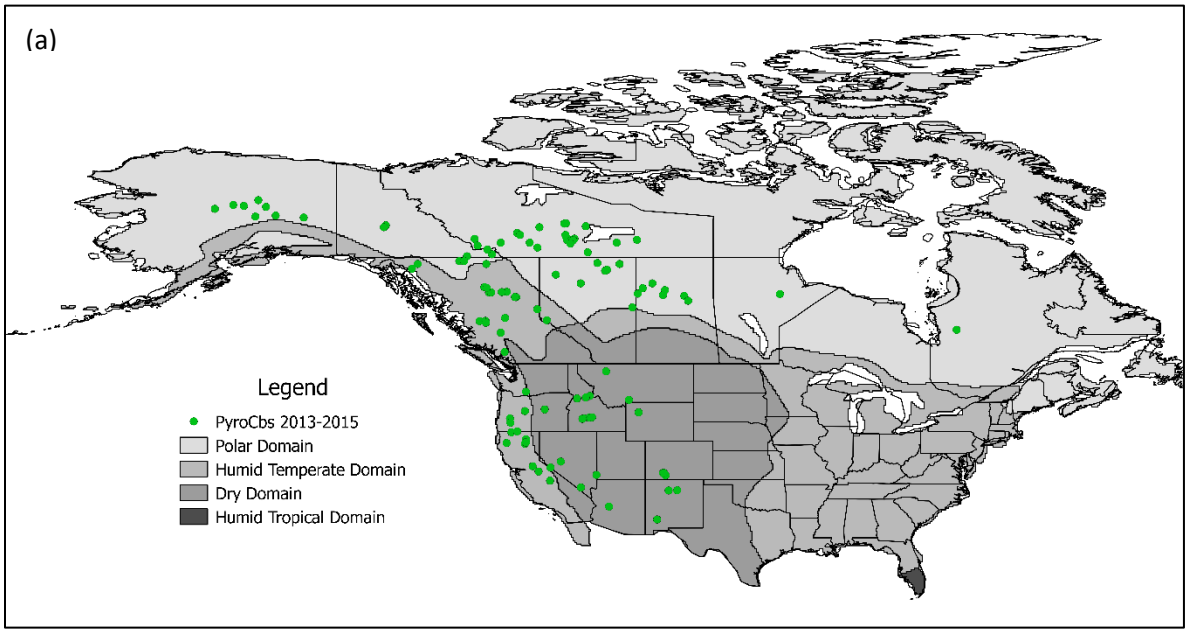

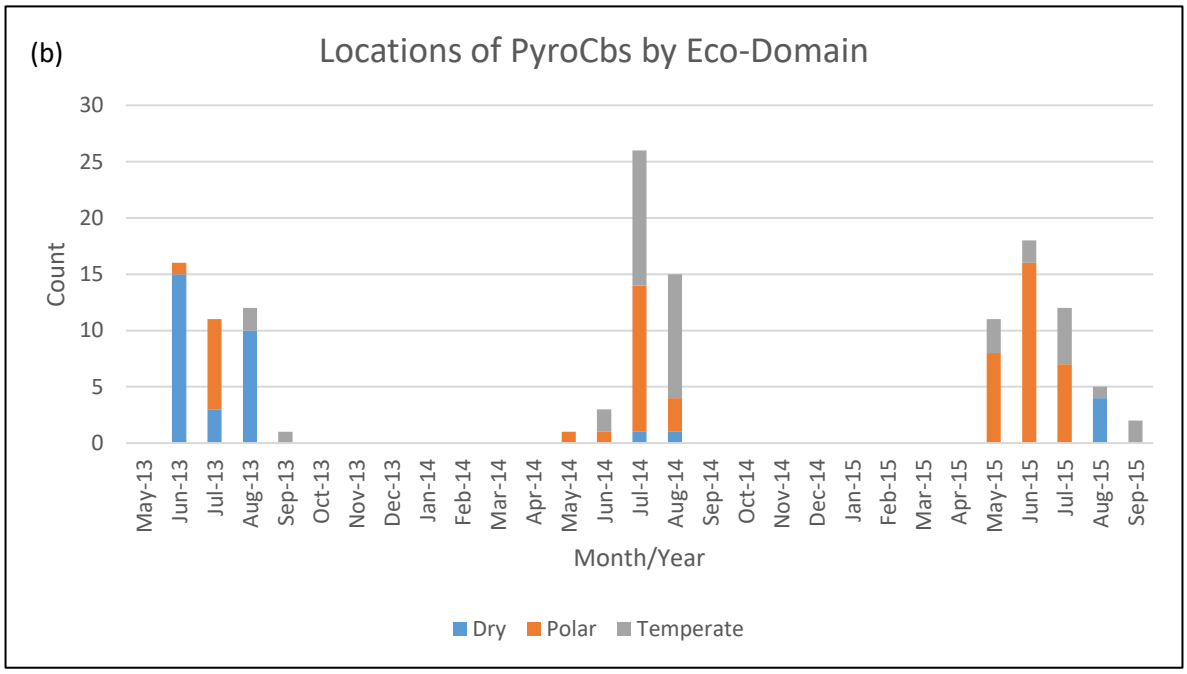

Figure 10a: Locations of PyroCbs between 2013 and 2015.

Figure 10b: PyroCb development by eco-domain.

Based on the results from this study, PyroCbs did not necessarily develop more frequently with more burn time. Figure 11a represents the frequency of PyroCbs during the 3 year timeframe against the number of days that had passed since the fire began (essentially PyroCb initiation date vs days of burning until convection). The days since start of the fire are binned to more easily display the results. As Figure 11a shows, 70 PyroCbs

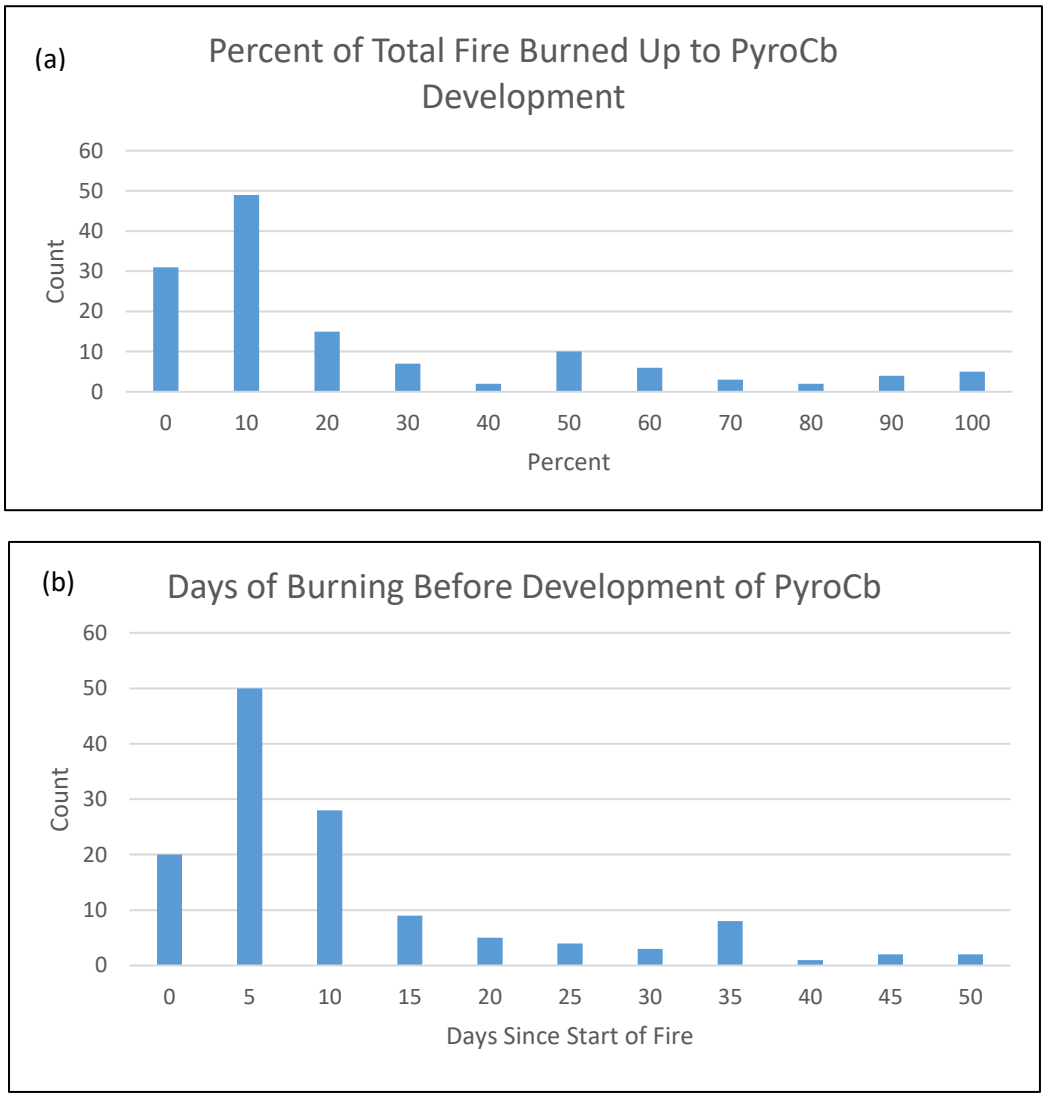

Figure 11a: Representation of the number of days a fire burns before producing a PyroCb. Most PyroCbs develop within the first 5 days of a fire's lifetime.

Figure 11b: Percentage of the total area burned before a PyroCb was produced, showing that most PyroCbs develop early in the lifetime of fires, regardless of the fire's actual lifetime.

were initiated between 0 and 5 days of the start of a forest fire, accounting for 52% of the total number of PyroCbs. The results suggest that the PyroCbs from this study tended to form early in the lifetime of a forest fire.

It could be argued that Figure 11a does not take into account short-lived fires; if most fires only burned a few days, then it will skew the results. Figure 11b is an attempt to reconcile that argument, as it displays the frequency of PyroCb initiation against the percentage of total fire area burned up until the development of the PyroCb. The results from this analysis make a stronger case for PyroCbs occurring early in the lifetime of forest fires. For nearly 80 of the PyroCb instances, less than 10% of a fire's eventual total burn scar area had been detected by the time the deep convection occurred. The initiation of a PyroCb early in the lifetime of a fire is consistent with the theories behind forest fires and PyroCb development. Pu et al. demonstrated that hot and dry conditions is a conducive environment for forest fires [Pu et al. 2007]. In Peterson et al. 2016, hot, dry, and windy conditions are required at the surface to initiate convection. Extremely dry and hot conditions are often observed before large wildfires occur, which can set the stage for PyroCb development even early in a fire's lifetime [Cruz et al., 2012].

Investigations into each of these PyroCb events is necessary to understanding the general conditions in which the storms occur. Examining the burn area sizes of PyroCbs indicated that the deep convection often develops early in a forest fire's lifetime. Other meteorological parameters, such as those laid out in Peterson et al., 2016 and described earlier here, may be the driving force behind the strong convection, and a fire at the surface is a trigger for the events.

3.3 PyroCb Case Study

On July 31st, 2014, five PyroCbs developed in Northern California and Southern Oregon. The case study presented here was chosen for several reasons. For one, the development of all five PyroCbs was detected by the GOES-W satellite, allowing for tracking of the convection over time. The method of using GOES to detect and confirm PyroCbs has been used effectively in the past [Peterson et al. 2015; Peterson et al. 2017]. In addition, all five PyroCbs were relatively close to two stations (Reno, NV and Medford, OR) that launch two radiosondes per day, which allows for an understanding of the atmospheric conditions leading up to and after the development of the PyroCbs. Finally, the PyroCbs occurred early in the burning period of the fires that caused them, supporting the idea that PyroCbs often form at the beginning of a fire's lifetime.

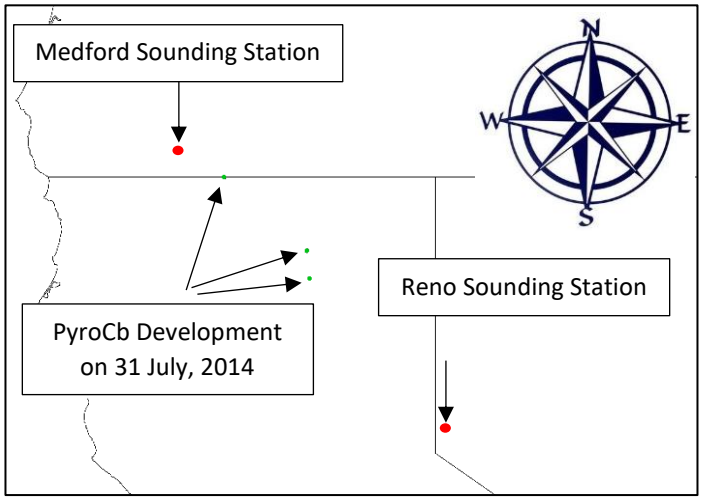

Figure 12: Locations of PyroCbs on 31 July, 2014 and two towns that release radiosondes twice a day.

Three fires, noted in Figure 12, provided energy for the development of 5 PyroCbs on July 31st, 2014. The two fires in Northern California produced two injections each between 20:30Z and 0400Z. Figure 13 is a quad-chart of (a) the GOES water vapor band, (b) the CFSR 12Z analysis, (c) the 12Z sounding from Medford, and (d) the 12Z sounding from Reno. At this time, the surface relative humidity from radiosonde data from Reno and Medford was observed around 56% and 68%, respectively. The CFSR 2m data estimated that the humidity at these stations to be slightly higher than the sounding values, but close

enough to make a comparison. At the location of the two fires in Northern California (noted on 13a and 13b), a lower relative humidity was estimated, which allows the fires to continue or enhance. While no sounding data was available at 18Z, the CFSR data at 2m above ground level (Figure 14b) shows much of Northern California had dried out, with relative humidity values around 20%.

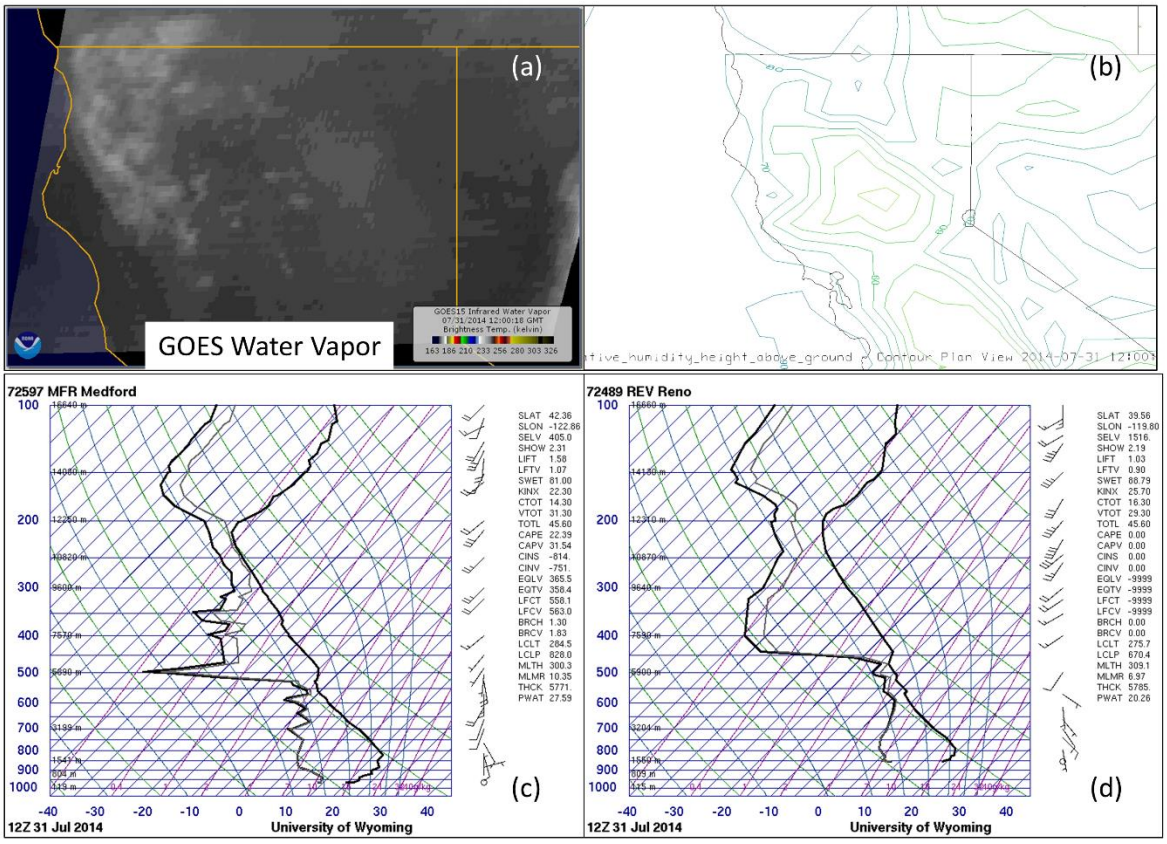

Figure 13: (a) GOES Water Vapor Imagery (b) CFSR 2m above ground level relative humidity, (c) Medford, OR Sounding, and (d) Reno,NV Sounding at 12Z on 31 July.

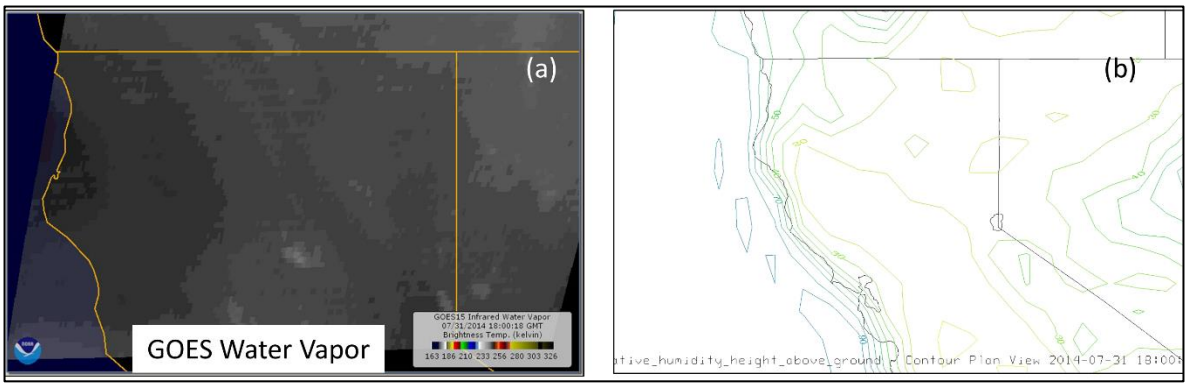

Figure 14: (a) GOES Water Vapor Imagery and (b) CFSR 2m above ground relative humidity at 18Z. No sounding was available at this time.

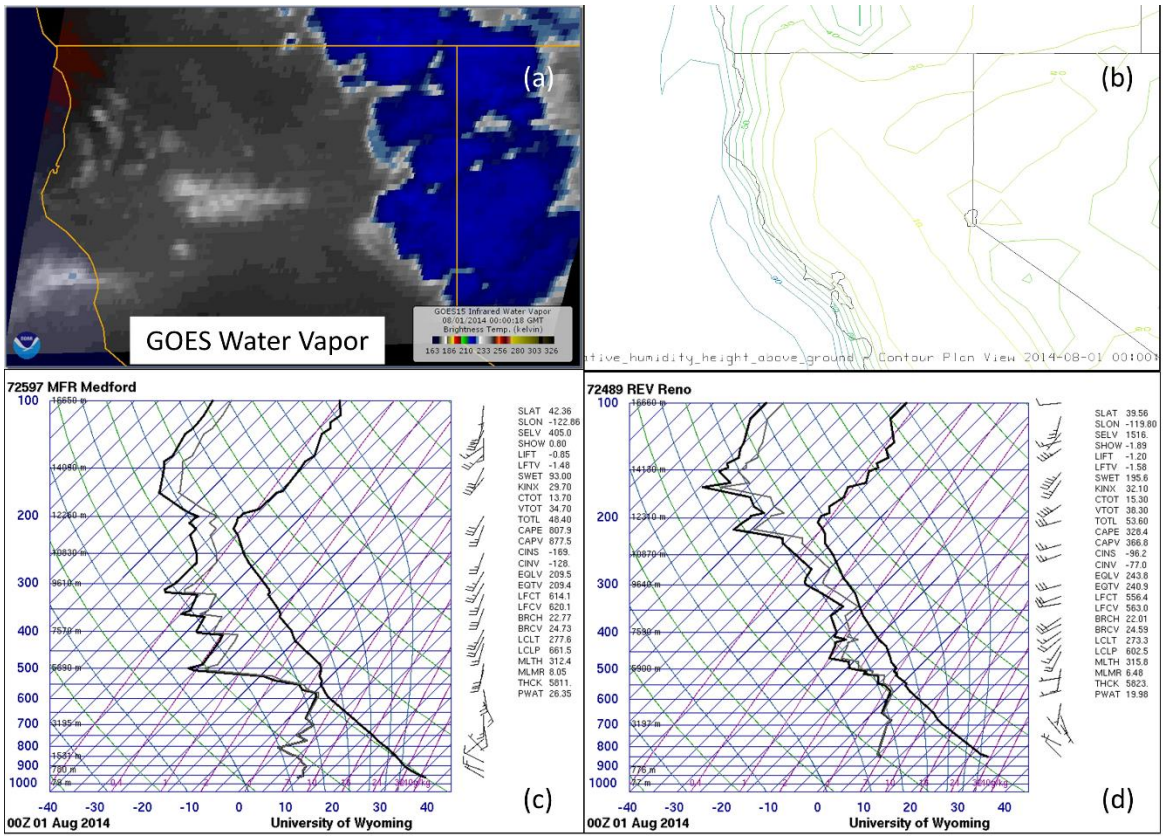

Figure 15: (a) GOES Water Vapor Imagery, (b) CFSR 2m above ground level relative humidity, (c) Medford, OR sounding, and (d) Reno, NV Sounding at 00Z on 1 August

The dry surface conditions continued until past 00Z on 1 August, which was after the development of the first PyroCbs. Figure 15 is like Figure 13, but at 00Z on 1 August. The sounding data and the modeled reanalysis are in good agreement; both have surface relative humidity values around 20% for the Reno and Medford regions. Little variation exists between the two stations according to the CFSR data, and dry conditions are persistent throughout. The surface is also hot, with temperatures at Reno reaching almost 30°C at 00Z, and Medford at 35°C at the same time. The conditions that exist at the surface lay the foundation for PyroCb development, but the thermodynamics and conditions of the middle atmosphere will be the deciding factor for formation [Peterson et al., 2016].

At 12Z, the mid-atmosphere at 550 hPa had considerably more water content than the surface level. Figure 16a-d is another quad-chart similar to Figures 13 and 15, but for

the 550 hPa at 12Z rather than for the surface level. At both Reno and Medford (and the area in between the two), the relative humidity is high; roughly 80% for both locations. The high moisture content continued throughout the day, and by 18Z a tight gradient of the moisture content is reproduced in the CFSR data, and slightly visible in the water vapor imagery from GOES (Figure 17a and 17b). After the first PyroCbs developed (which was around 2030Z), high moisture at the 550 hPa level persisted, and a very tight gradient in relative humidity was observed that extended from Medford down to Reno, and is reflected in their 00Z sounding data (Figure 18a-d). While the hot and dry surface conditions combined with the consistently moist mid-level provided a means for deep convection to occur, the fires that burned at the surface provided the trigger that initiated 5 PyroCbs to develop over the course of a few hours. Time lapse GOES imagery will be included in the Appendix to showcase the development of the PyroCbs.

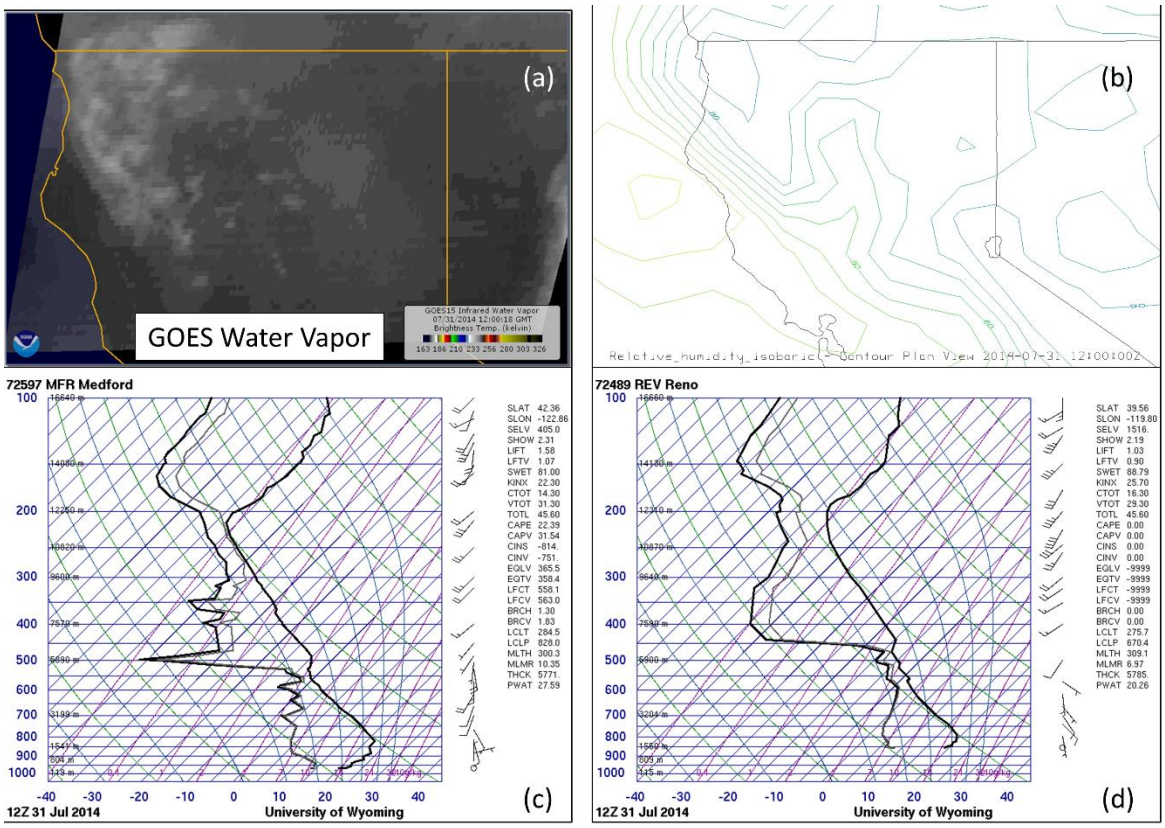

Figure 16: (a) GOES Water Vapor Imagery (b) CFSR 550 hPa relative humidity, (c) Medford, OR Sounding, and (d) Reno, NV Sounding at 12Z on 31 July

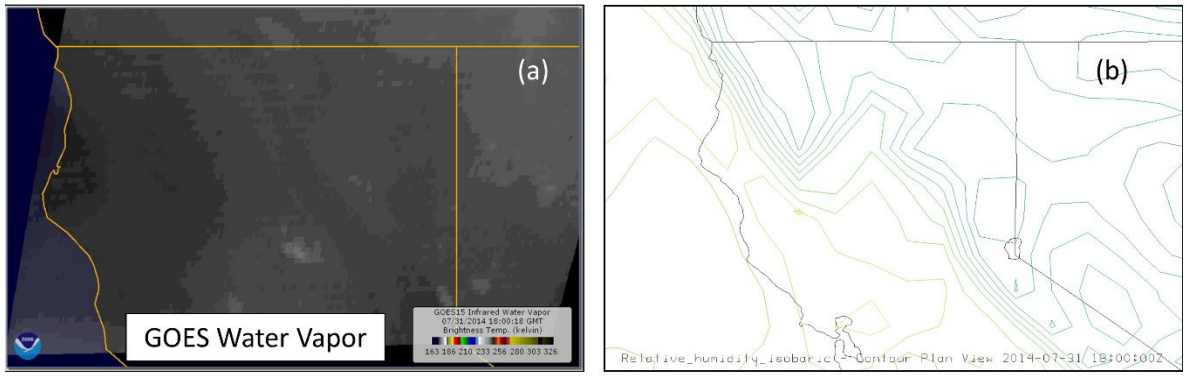

Figure 17: (a) GOES Water Vapor Imagery and (b) CFSR 550 hPa relative humidity at 18Z on 31 July

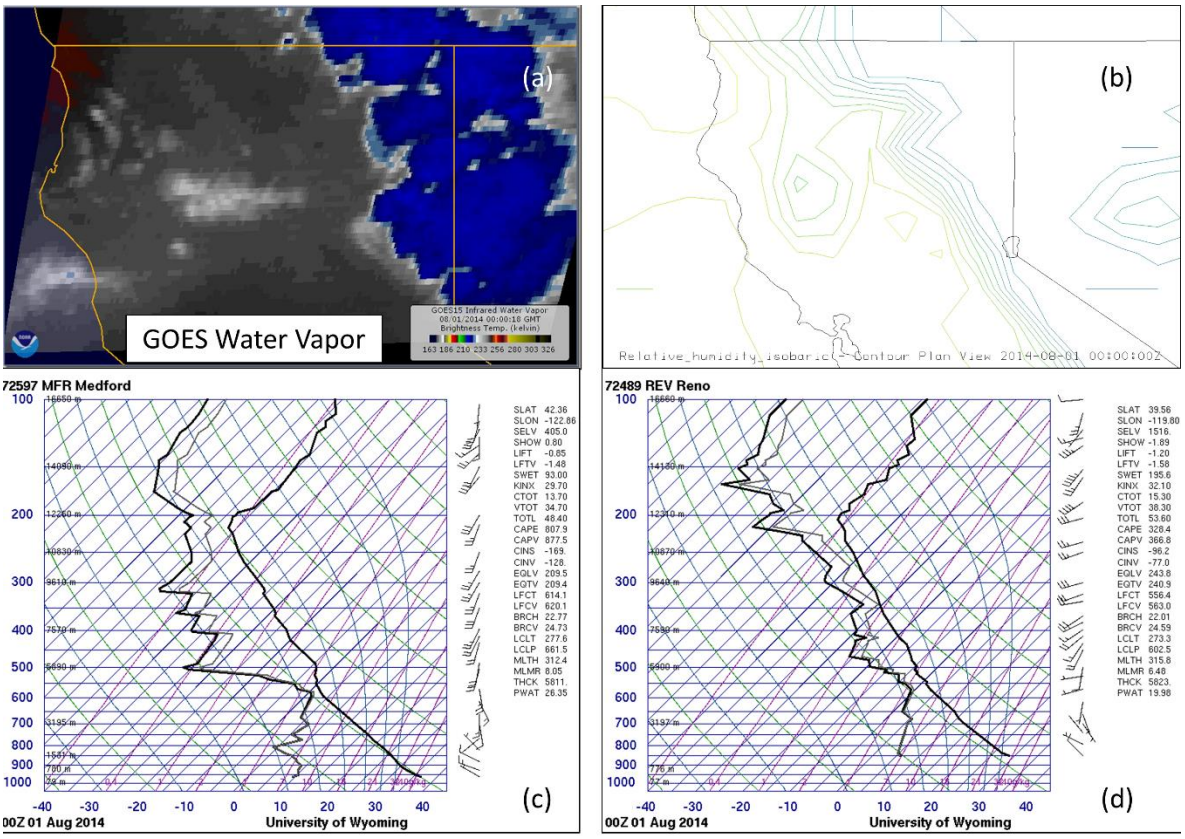

Figure 18: (a) GOES Water Vapor Imagery (b) CFSR 550 hPa relative humidity, (c) Medford, OR Sounding, and (d) Reno, NV Sounding at 00Z on 01 August

Section 4: Summary

The research covered in this paper focuses on the amount of burn scar area between 2002 and 2015 in North America, and then connections between fire size and PyroCb development. Between the years of interest, an average of 6.3 x 10^4 km^2 of burn scars were detected with the MODIS burn scar product. 2014 experienced the highest amount of burning, with 9.0 x 10^4 km^2 of burn scar detected. The lowest amount of burning occurred in 2009, where only 2.8 x 10^4 km^2 burned. In the time of the study, July, on average, was the peak burning month, and May was the month with the least amount of burn scar in North America. The values arrived at in this study are higher than the values obtained from

similar studies, but within the same order of magnitude. The discrepancies could be due to the fact that the research here included the use of two satellites, MODIS/Terra and MODIS Aqua, while other studies in the past have only used one satellite [Pu et al., 2007; Giglio et al., 2006]. However, there could be other errors involved in the methods presented here, which could lead to an overestimation of annual burn scar area. Future work will attempt to compare results with modeled values of burn scar to validate the method.

In connection to PyroCbs, it was determined that PyroCbs can develop at any point in a wildfire's lifetime, but they typically form early; within the first few days or 10% of burning. The early development may be due the meteorological parameters at the surface being conducive to both PyroCb development and forest fire propagation. At the surface, the hot, dry, and windy conditions allows the fire to spread and provides energy for PyroCb development if the smoke, aerosols, and heat reaches a moist mid-layer in the atmosphere [Peterson et al., 2016]. Future work will attempt to incorporate more PyroCb cases, working back from 2013. With a larger sample size, a better idea of the surface conditions required for PyroCb development will add confidence to the theories surrounding their formation.

In addition, a brief study case was examined to understand the meteorological parameters surrounding the creation of five PyroCbs within one day in 2014. Using GOES satellite imagery, in-situ observations, and CFSR data, the thermodynamic properties (including relative humidity and temperature) were tracked throughout the development of the storms. As was conceptualized in Peterson et al. 2016, hot and dry conditions at the surface mixed with a moist middle layer set the stage for the PyroCbs to form. Consistent with the results from the research in this study, these PyroCbs developed early in the

lifetime of the wildfires; within the first 2 days of detection from MODIS. To confirm the current understanding of necessary conditions for the formation of these storms, more case studies will be examined in future work.

There is still much work to be done in both biomass burning and PyroCb research. Under a climate change scenario, the future of both phenomenon is uncertain as each not only impacts climate but also are impacted by a changing climate. For example, it is expected that burning seasons in temperate and polar regions will increase in a warming world [Flannigan et al., 2009]. The research conducted here has shown that polar regions already contribute the most to burn area for North America, and increasing the burn season will have devastating impacts to local habitats. The future of PyroCbs is still unknown. Currently, it is thought that the contribution of PyroCbs to global climate is underestimated [Peterson et al., 2017]. In a warmer climate with extended burning seasons in polar and temperate regions, it is possible that PyroCb activity will increase in the near future. We are in a unique position with the availability of satellite, in-situ, and modeled data to understand completely the climatological impacts of events like PyroCbs. Future research in this field is vital to a total understanding of the Earth System and its many complex mechanisms.

Citations

Akagi, S. K., Yokelson, R. J., Wiedinmyer, C., Alvarado, M. J., Reid, J. S., Karl, T., . . . Wennberg, P. O. (2011). Emission factors for open and domestic biomass burning for use in atmospheric models. *Atmospheric Chemistry and Physics, 11*(9), 4039-4072. doi:10.5194/acp-11-4039-2011

Boschetti, L., Roy, D., Hoffmann, Anja., Humber, M. (2013) *MODIS Collection 5.1 Burned Area Product – MCD45*

Boucher, O., D. Randall, P. Artaxo, C. Bretherton, G. Feingold, P. Forster, V.-M. Kerminen, Y. Kondo, H. Liao, U. Lohmann, P. Rasch, S.K. Satheesh, S. Sherwood, B. Stevens and X.Y. Zhang, 2013: Clouds and Aerosols. In: Climate Change 2013: The Physical Science Basis. Contribution of Working Group I to the Fifth Assessment Report of the Intergovernmental Panel on Climate Change [Stocker, T.F., D. Qin, G.-K. Plattner, M. Tignor, S.K. Allen, J. Boschung, A. Nauels, Y. Xia, V. Bex and P.M. Midgley (eds.)]. Cambridge University Press, Cambridge, United Kingdom and New York, NY, USA.

Cruz, M. G., Sullivan, A. L., Gould, J. S., Sims, N. C., Bannister, A. J., Hollis, J. J., & Hurley, R. J. (2012). Anatomy of a catastrophic wildfire: The Black Saturday Kilmore East fire in Victoria, Australia. *Forest Ecology and Management, 284*, 269-285. doi:10.1016/j.foreco.2012.02.035

Dozier, J. (1981). A METHOD FOR SATELLITE IDENTIFICATION OF SURFACE-TEMPERATURE FIELDS OF SUBPIXEL RESOLUTION. *Remote Sensing of Environment, 11*(3), 221-229. doi:10.1016/0034-4257(81)90021-3

Flannigan, M. D., Krawchuk, M. A., de Groot, W. J., Wotton, B. M., & Gowman, L. M. (2009). Implications of changing climate for global wildland fire. *International Journal of Wildland Fire, 18*(5), 483-507. doi:10.1071/wf08187

Flannigan, M. D., & Wotton, B. M. (1991). LIGHTNING-IGNITED FOREST-FIRES IN NORTHWESTERN ONTARIO. *Canadian Journal of Forest Research-Revue Canadienne De Recherche Forestiere, 21*(3), 277-287. doi:10.1139/x91-035

Fromm, M., Bevilacqua, R., Servranckx, R., Rosen, J., Thayer, J. P., Herman, J., & Larko, D. (2005). Pyro-cumulonimbus injection of smoke to the stratosphere: Observations and impact of a super blowup in northwestern Canada on 3-4 August 1998. *Journal of Geophysical Research-Atmospheres, 110*(D8), 16. doi:10.1029/2004jd005350

Fromm, M., Lindsey, D. T., Servranckx, R., Yue, G., Trickl, T., Sica, R., . . . Godin-Beekmann, S. E. (2010). THE UNTOLD STORY OF PYROCUMULONIMBUS. *Bulletin of the American Meteorological Society, 91*(9), 1193-1209. doi:10.1175/2010bams3004.1

Fromm, M., Shettle, E. P., Fricke, K. H., Ritter, C., Trickl, T., Giehl, H., . . . Deshler, T. (2008). Stratospheric impact of the Chisholm pyrocumulonimbus eruption: 2. Vertical

profile perspective. *Journal of Geophysical Research-Atmospheres, 113*(D8), 19. doi:10.1029/2007jd009147

Giglio, Louis. (2015). *MODIS Collection 6 Active Fire Product User's Guide Revision A*, University of Maryland

Giglio, L., van der Werf, G. R., Randerson, J. T., Collatz, G. J., & Kasibhatla, P. (2006). Global estimation of burned area using MODIS active fire observations. *Atmospheric Chemistry and Physics, 6*, 957-974.

Justice, C., Giglio, L., Boschetti, L., Roy, D., Ivan, Csiszar., Morisette, J., Kaufman, Y. (2006). *MODIS Fire Products: Algorithm Technical Background Document*

Kasischke, E. S., Williams, D., & Barry, D. (2002). Analysis of the patterns of large fires in the boreal forest region of Alaska. *International Journal of Wildland Fire, 11*(2), 131-144. doi:10.1071/wf02023

Kaufman, Y. J., Justice, C. O., Flynn, L. P., Kendall, J. D., Prins, E. M., Giglio, L., . . . Setzer, A. W. (1998). Potential global fire monitoring from EOS-MODIS. *Journal of Geophysical Research-Atmospheres, 103*(D24), 32215-32238. doi:10.1029/98jd01644

Matson, M., & Dozier, J. (1981). IDENTIFICATION OF SUBRESOLUTION HIGH-TEMPERATURE SOURCES USING A THERMAL IR SENSOR. *Photogrammetric Engineering and Remote Sensing, 47*(9), 1311-1318.

McRae, R. H. D., Sharples, J. J., & Fromm, M. (2015). Linking local wildfire dynamics to pyroCb development. *Natural Hazards and Earth System Sciences, 15*(3), 417-428. doi:10.5194/nhess-15-417-2015

Peterson, D. A., Fromm, M. D., Solbrig, J. E., Hyer, E. J., Surratt, M. L., & Campbell, J. R. (2017). Detection and Inventory of Intense Pyroconvection in Western North America using GOES-15 Daytime Infrared Data. *Journal of Applied Meteorology and Climatology, 56*(2), 471-493. doi:10.1175/jamc-d-16-0226.1

Peterson, D. A., Hyer, E. J., Campbell, J. R., Fromm, M. D., Hair, J. W., Butler, C. F., & Fenn, M. A. (2015). THE 2013 RIM FIRE Implications for Predicting Extreme Fire Spread, Pyroconvection, and Smoke Emissions. *Bulletin of the American Meteorological Society, 96*(2), 229-247. doi:10.1175/bams-d-14-00060.1

Peterson, D., E. Hyer, J. Campbell, J. Solbrig, and M. Fromm, 2016: A Conceptual Model for Development of Intense Pyrocumulonimbus in Western North America. Mon. Wea. Rev. doi:10.1175/MWR-D-16-0232.1, in press.

Pu, R. L., Li, Z. Q., Gong, P., Csiszar, I., Fraser, R., Hao, W. M., . . . Weng, F. Z. (2007). Development and analysis of a 12-year daily 1-km forest fire dataset across North America from NOAA/AVHRR data. *Remote Sensing of Environment, 108*(2), 198-208. doi:10.1016/j.rse.2006.02.027

Ramanathan, V., Crutzen, P. J., Kiehl, J. T., & Rosenfeld, D. (2001). Atmosphere - Aerosols, climate, and the hydrological cycle. *Science, 294*(5549), 2119-2124. doi:10.1126/science.1064034

Rosenfeld, D., Fromm, M., Trentmann, J., Luderer, G., Andreae, M. O., & Servranckx, R. (2007). The Chisholm firestorm: observed microstructure, precipitation and lightning activity of a pyro-cumulonimbus. *Atmospheric Chemistry and Physics, 7*, 645-659.

Roy, D., Borak, J, Devadiga, S., Wolfe, R., Zheng, M., Descloitres, J., (2002), The MODIS land product quality assessment approach, *Remote Sensing of Environment*, 83:62-76.

Roy, D. P., Boschetti, L., Justice, C. O., & Ju, J. (2008). The collection 5 MODIS burned area product - Global evaluation by comparison with the MODIS active fire product. *Remote Sensing of Environment, 112*(9), 3690-3707. doi:10.1016/j.rse.2008.05.013

Roy, D.P., Jin, Y., Lewis, P.E., Justice, C.O., (2005), Prototyping a global algorithm for systematic fire-affected area mapping using MODIS time series data, *Remote Sensing of Environment*, 97: 137-162.

L. Thomason and Th. Peter (Eds.).SPARC, 2006: SPARC Assessment of Stratospheric Aerosol Properties (ASAP)., SPARC Report No. 4, WCRP-124, WMO/TD - No. 1295, available at www.sparc-climate.org/publications/sparc-reports/

Twomey, S. (1974). POLLUTION AND PLANETARY ALBEDO. *Atmospheric Environment, 8*(12), 1251-1256. doi:10.1016/0004-6981(74)90004-3

Wallace, J. M., & Hobbs, P. V. (2006). *Atmospheric science: An introductory survey*. Amsterdam: Elsevier Academic Press.

Wierzchowski, J., Heathcott, M., & Flannigan, M. D. (2002). Lightning and lightning fire, central cordillera, Canada. *International Journal of Wildland Fire, 11*(1), 41-51. doi:10.1071/wf01048

Appendix

Date	Latitude	Longitude	Name		Date	Latitude	Longitude	Name
20130604	35.887	-106.62	Thompson Ridge		20130812	43.294	-115.548	Pony
20130604	56	-105	NA		20130813	43.294	-115.548	Pony
20130611	35.911	-105.728	Jaroso		20130816	45.657	-114.78	Gold Pan Complex
20130612	32.893	-107.81	Silver		20130816	43.457	-114.55	Beaver Creek Complex
20130613	32.893	-107.81	Silver		20130818	38.263	-118.85	Spring Peak
20130619	37.461	-106.944	West Fork		20130818	38.877	-117.787	Chestnut
20130620	37.461	-106.944	West Fork		20130819	37.857	-120.086	Rim
20130621	37.461	-106.944	West Fork		20130819	45.249	-110.733	Emigrant
20130621	37.7	-107.21	West Fork/Papoose		20130821	37.857	-120.086	Rim
20130623	37.461	-106.944	West Fork		20130915	53.4	-126.2	NA
20130626	37.461	-106.944	West Fork Complex		20140523	55.5	-104.6	NA
20130627	32.893	-107.81	Silver		20140602	56.9	-125.7	NA
20130628	32.893	-107.81	Silver		20140608	44.1	-121.5	Two Bulls
20130628	37.461	-106.944	West Fork		20140614	59.4	-114	NA
20130630	32.893	-107.81	Silver		20140702	37.5	-114.1	NA
20130630	34.225	-112.791	Yarnell Hill		20140714	61.8	-116.68	NA
20130703	60.3	-124.9	NA		20140714	61.77	-116.97	NA
20130703	56.2	-95.1	NA		20140714	56.35	-125.23	NA
20130703	37.7	-107.1	West Fork/Papoose		20140714	55.87	-122.43	NA
20130704	52.5	-76.8	NA		20140714	53.42	-125.58	NA
20130704	36.202	-115.702	Carpenter 1		20140714	57.3	-115.72	NA
20130708	62.5	-122.3	NA		20140714	63.47	-117.43	NA
20130708	61	-120.2	NA		20140714	62.07	-117.22	NA
20130709	61.5	-112	NA		20140715	54.63	-120.22	NA
20130715	63.3	-135.9	NA		20140715	56.36	-125	NA
10130725	63.1	-120	NA		20140715	55.87	-122.4	NA
20130726	43.967	-109.728	Hardluck		20140715	56.84	-125.45	NA
20130808	43.457	-114.55	Beaver Creek		20140715	61.92	-116.37	NA
20130808	43.42	-114.852	McCan		20140715	61.78	-117.13	NA
20130810	43.358	-115.448	Elk		20140723	61.75	-116.5	NA

Date	Latitude	Longitude	Name
20140723	63.5	-117.25	NA
20140726	61.75	-116.5	NA
20140726	63.2	-115.2	NA
20140729	61.5	-121	NA
20140730	61.75	-116.5	NA
20140731	41.2	-121.4	NA
20140731	40.9	-121.37	Bald
20140731	42	-122.3	NA
20140731	41.2	-121.4	NA
20140731	42	-122.3	NA
20140801	40.9	-121.37	Bald
20140801	40.72	-121.5	Eiler
20140801	42	-122.3	Beaver Complex
20140801	53.23	-125.54	NA
20140802	41.9	-122.9	NA
20140802	42	-122.3	NA
20140802	40.85	-121.4	NA
20140802	53.23	-125.54	NA
20140804	61.41	-116.8	NA
20140805	60.5	-115	NA
20140805	61.8	-109.9	NA
20140809	44.27	-119.45	South Fork Complex
20140811	43.34	-123.05	July Complex
20140812	56.42	-123.38	NA
20140812	55.88	-122.53	NA
20150512	53.72	-123.55	Little Bobtail Lake
20150520	59.3	-125.5	NA
20150522	56.23	-109.82	15BN-David
20150522	54.81	-110.37	LWF-122-2015
20150525	56.23	-109.82	15BN-David
20150525	59.3	-132.6	R90047
20150530	61.9	-126.7	NA
20150530	60.8	-125.4	NA
20150530	62.3	-122	FS018-15
20150530	61.5	-124	NA
20150530	61.2	-126.4	NA
20150605	58.6	-113.2	NA
20150605	58.6	-113.2	NA
20150606	58.6	-113.2	NA
20150611	53.49	-119.24	EWF-054-2015
20150620	64.1	-144.4	Michigan Creek
20150621	65.3	-150.6	NA
20150622	64.2	-149.4	Kobe
20150622	65.9	-149.1	NA
20150623	65.4	-151.7	NA
20150623	65.2	-148.3	NA
20150623	65	-153.6	NA
20150623	58.8	-133.2	R90046
20150624	64.3	-147.3	Blair
20150624	56.8	-109.3	15BN-BRADY
20150625	62.3	-117.3	ZF010-15
20150625	63.1	-136.1	NA
20150626	58.7	-113	NA
20150626	59.3	-111.7	NA
20150702	60.1	-127.5	2015WL018
20150702	59.6	-128.3	R90045
20150702	59.6	-127.8	G90180
20150703	56.1	-107.2	15XL-FORCIER
20150703	56.6	-107	15XL-PORTER
20150703	57.3	-108.3	NA
20150703	58.2	-118.3	HWF-219-2015
20150705	50.2	-123.6	V30160
20150710	56.4	-123.9	NA
20150710	52.2	-124	Puntzi Lake
20150730	42.9	-123	Stouts
20150731	40.8	-123.4	River Complex
20150812	46.1	-121.4	Cougar Creek
20150826	45.5	-115.2	Campbells
20150826	45.4	-116.1	Tepee Springs
20150827	45.4	-116.1	Tepee Springs
20150828	48.2	-113.1	Family Peak Complex
20150910	38.4	-120.7	Buttte
20150911	36.9	-118.9	Rough

Table 2: A list of all 133 PyroCbs used in this study detected between 2013 and 2015. These were compiled from the PyroCb database maintained by the PyroCb Working Group.

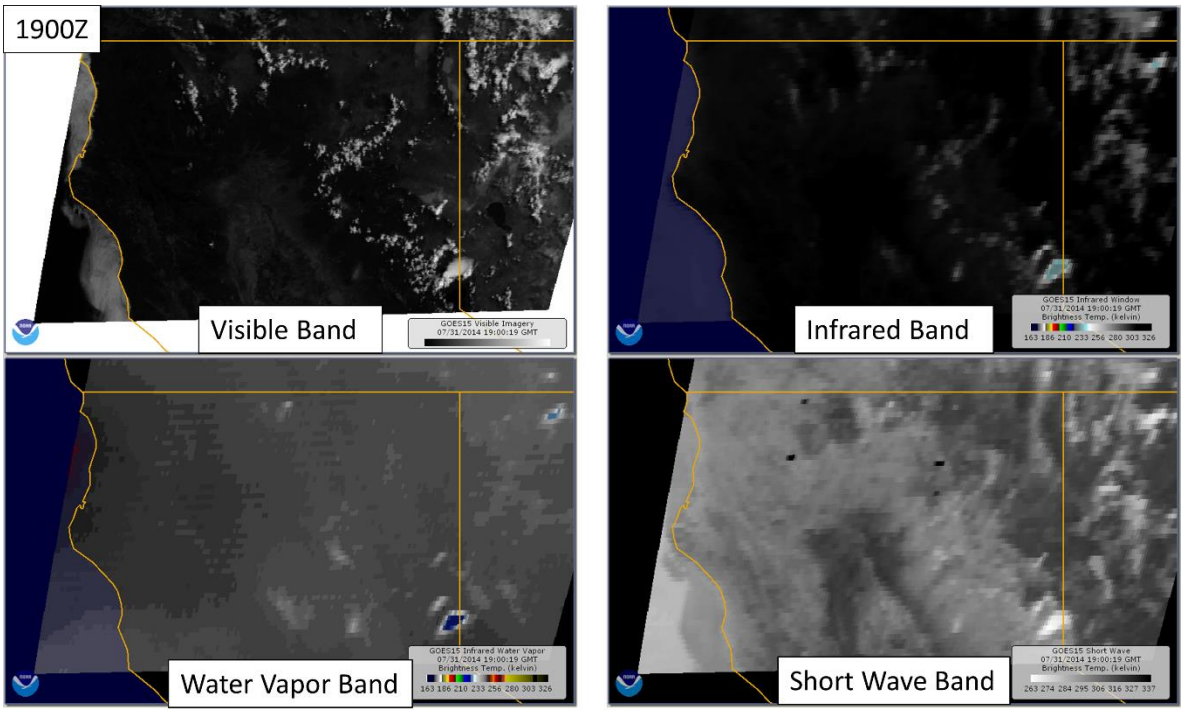

Figure 19: GOES Imagery at 19Z, before initiation of PyroCb

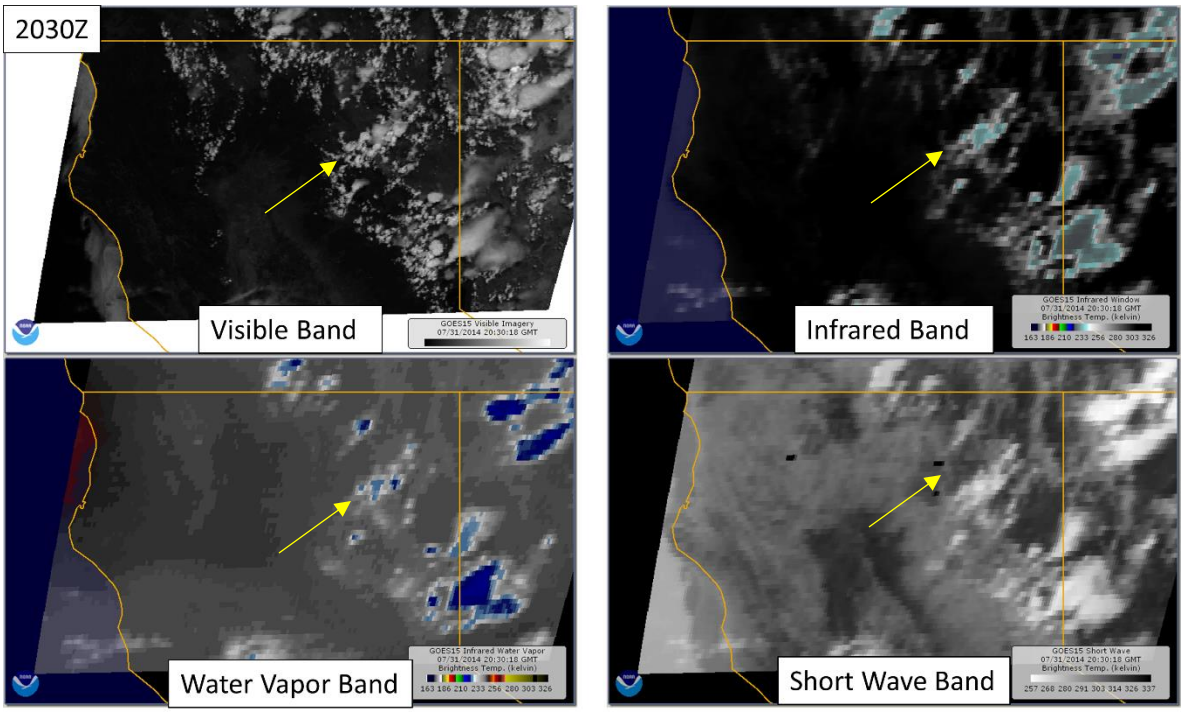

Figure 20: GOES Imagery at 2030Z as the first of the PyroCbs are developing at area indicated by the yellow arrow.

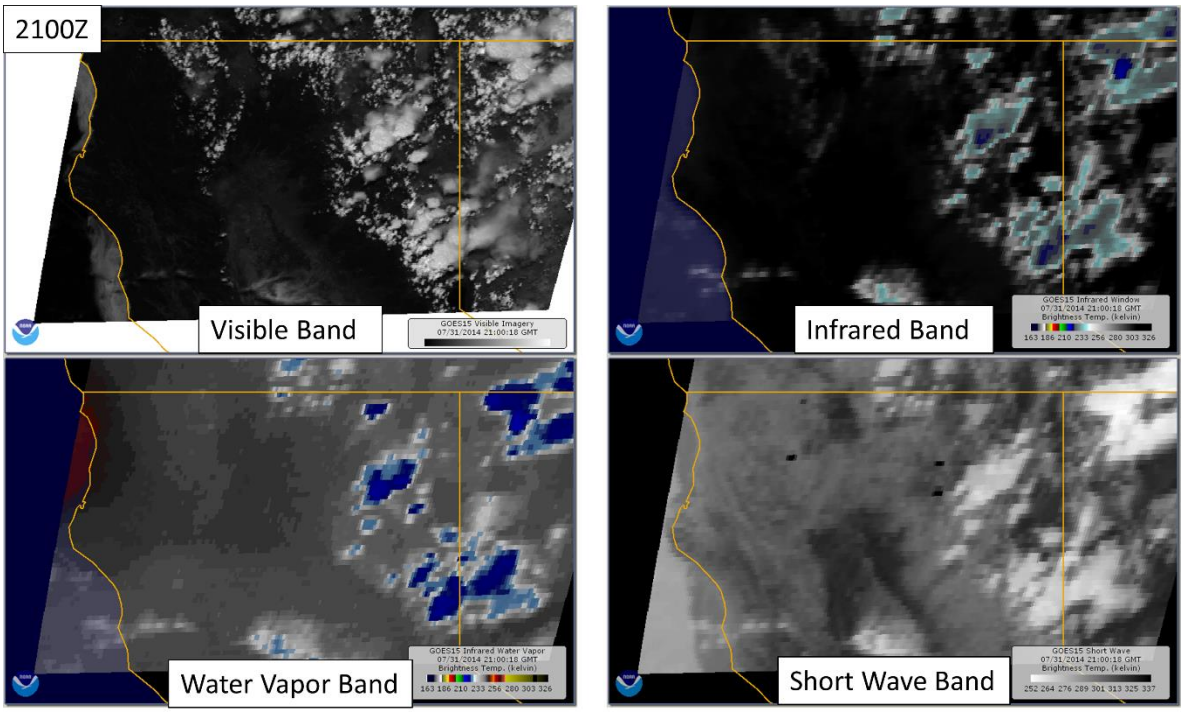

Figure 21: GOES Imagery at 21Z after the development of the first PyroCb.

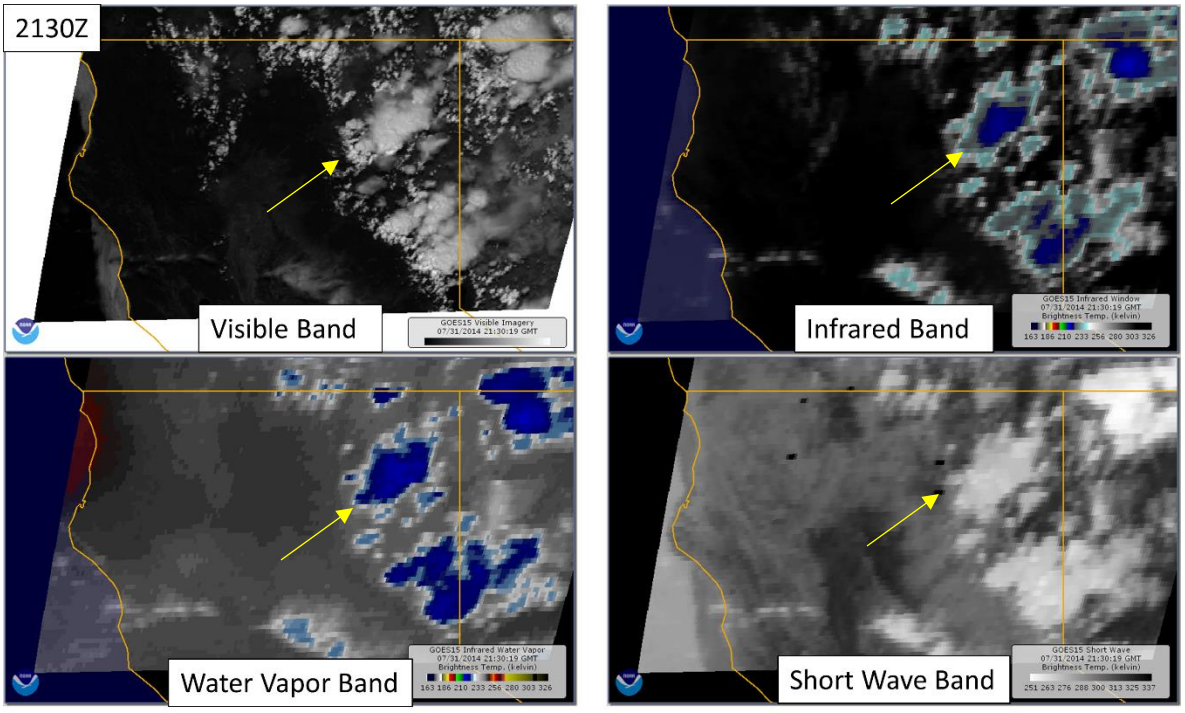

Figure 22: GOES Imagery at 2130 as the second PyroCb develops (yellow arrows) and as the plume from the first PyroCb is spreading and becoming colder.

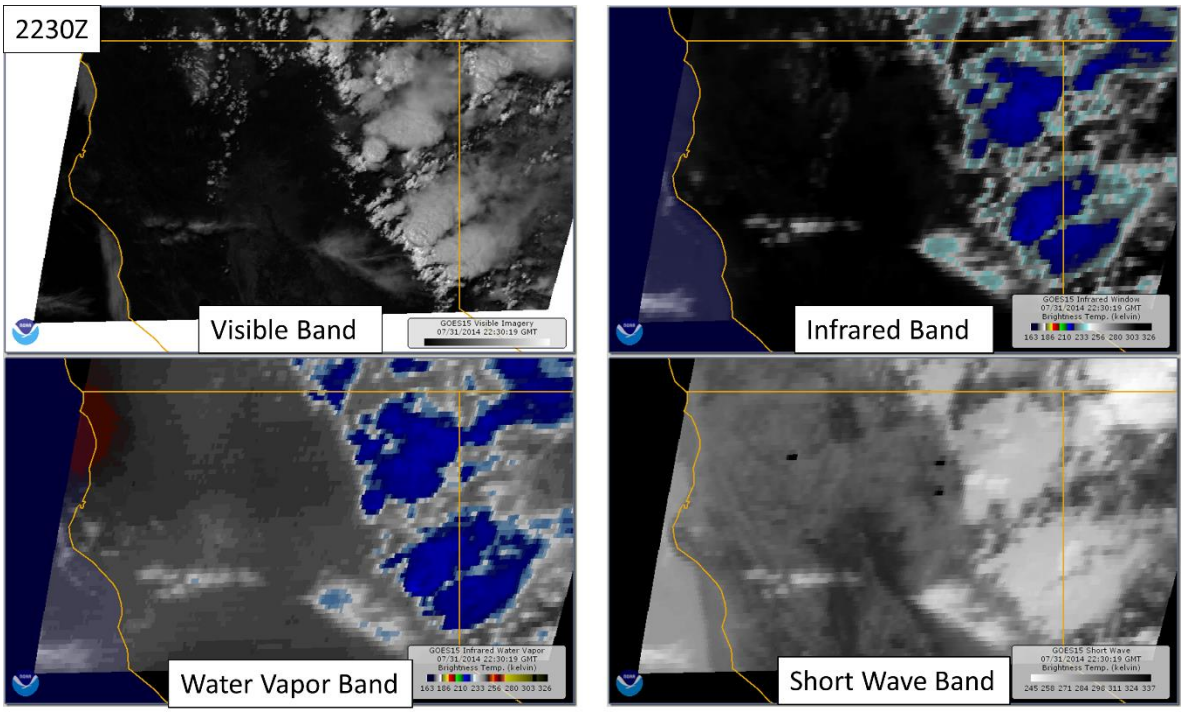

Figure 23: GOES Imagery from 2230Z as the plumes from both PyroCbs are rising and cooling.

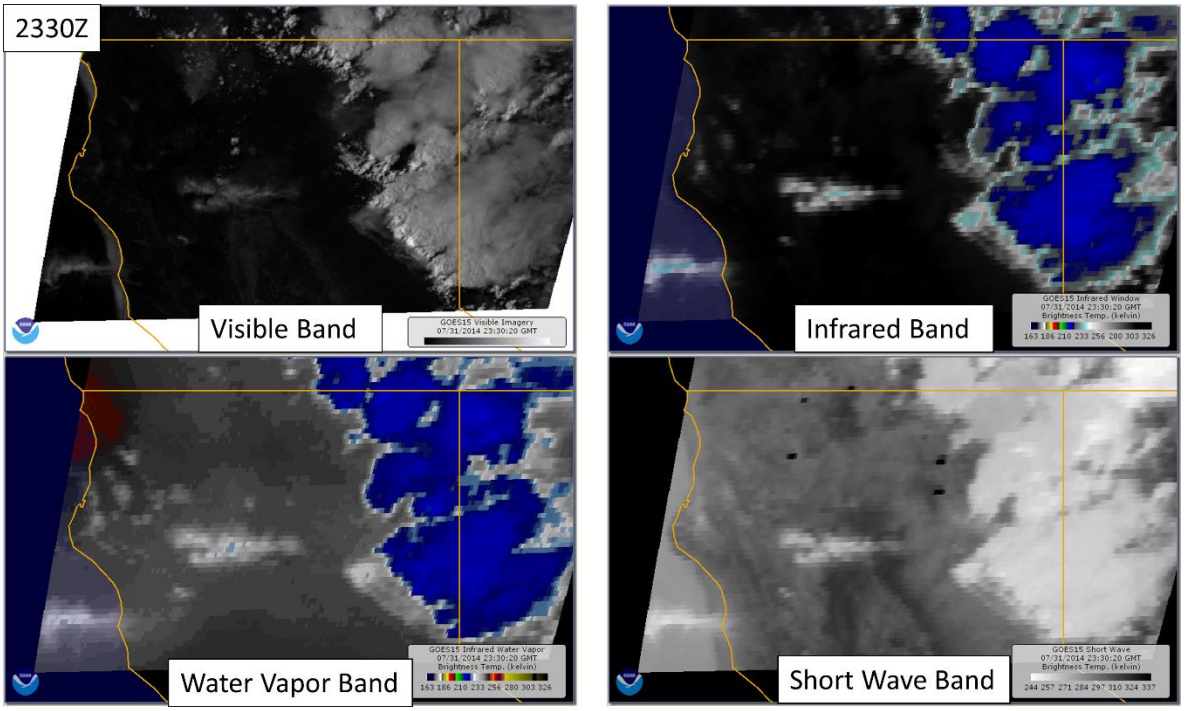

Figure 24: GOES Imagery at 2330Z. The plume from the first PyroCb has reached a minimum temperature of - 57°C and is roughly 11.7 km based on the Medford Sounding. Non-PyroCb convection is occurring in the area as well.